A descending pathway through electrical coupling facilitates undulatory wave propagation in *C. elegans*

Tianqi Xu[1,3], Jing Huo[1,3], Shuai Shao[1], Michelle Po[2], Taizo Kawano[2], Yangning Lu[2], Min Wu[2], Mei Zhen[2], Quan Wen[1,*]

1. Chinese Academy of Sciences Key Laboratory of Brain Function and Disease, School of Life Sciences, Center for Excellence in Brain Science and Intelligence Technology, University of Science and Technology of China, Hefei, 230027, China

2. Lunenfeld-Tanenbaum Research Institute, Mount Sinai Hospital, University of Toronto, Toronto, ON, Canada

3. These authors contribute equally to this work

*Corresponding author: qwen@ustc.edu.cn

Descending signals from the brain play critical roles in controlling and modulating locomotion kinematics. The anatomical wiring diagram of the *C. elegans* nervous system suggests that the premotor interneurons AVB, the hub for sensorimotor transformation, make exclusively electrical synapses with the B-type motor neurons that activate body wall muscles and drive forward locomotion. Here, we combined genetic analysis, optogenetic manipulation, and computational modeling to elucidate the functions of AVB-B electrical couplings. First, we found that B-type motor neurons could intrinsically generate rhythmic activity, constituting distributed center pattern generators. Second, AVB-B electrical couplings provide a descending pathway to drive bifurcation of motor neuron dynamics, triggering their transition from being stationary to generating rhythmic activity. Third, directional proprioceptive couplings between neighboring B-type motor neurons entrain the undulation frequency, forcing coherent bending waves to propagate from head to tail. Together, we propose that AVB-B electrical couplings work synergistically with proprioceptive couplings to enhance sequential activation of motor activity, and to facilitate the propagation of body undulation from head to tail during *C. elegans* forward locomotion.

Descending pathway; motor control; central pattern generator (CPG); *C. elegans*; optogenetics; proprioception; gap junction

Introduction

Locomotion requires coordinated rhythmic motor activity. In vertebrate and invertebrate motor systems, oscillatory signals are generated by dedicated neural circuits with intrinsic rhythmic properties called center pattern generator (CPG) [1-6]. Distributed CPG modules, which correspond to different body segments, drive muscle movement with defined spatial patterns and temporal sequences. Coordination of rhythmic movement throughout the animal's body requires a coupling mechanism, by which the dynamics of individual CPGs are both frequency and phase-locked [5, 7].

United efforts have been carried out, by using different model systems, to define the circuit logic for driving, modulating and coordinating locomotion [8, 9]. The execution and maintenance of locomotion in vertebrates require descending signals from the brainstem and other brain regions, where glutamatergic neurons make connections with spinal premotor interneurons or establish direct synaptic contacts with motor neurons [10]. For example, descending reticulospinal neurons driving excitatory neurons could initiate locomotion and modulate the speed of locomotion [11-13], whereas those activating groups of inhibitory neurons in the spinal cord could terminate locomotion [14]. Descending neurons directly targeting forelimb motor neurons are critical for skillful motor behaviors [15].

Besides chemical synaptic transmission, gap junction couplings are also prevalent in the invertebrate motor circuit as well as the vertebrate spinal cord [16-18]. In neonatal rats, electrical coupling between motor neurons was proposed to drive synchronized inputs to muscle cells [19]. In zebrafish, electrical coupling between motor neuron and premotor interneuron points to a nimbly feedback mechanism for modulating rhythmic activity [20]. These findings shed new light on the roles of electrical synapses in coordinating and controlling locomotion.

With a connectome at synaptic resolution and fully identified cell-types, *C. elegans* offers a unique opportunity to obtain a complete system-level understanding of a locomotory circuit. Here, we study the undulatory wave coordination during forward locomotion in *C. elegans*, addressing how command signals from the brain control the motor circuit. *C. elegans* locomotion is controlled by a network of excitatory cholinergic motor neurons, the A- and B-types that control backward and forward movement respectively, and inhibitory motor neurons (D-type) innervating body wall muscle cells [21]. The anatomical wiring diagram [22, 23] of the adult worm motor circuit has revealed that the premotor inter-neurons AVB, which receive numerous inputs from sensory and other inter-neurons, have long processes along the entire ventral nerve cord, and form exclusive gap junctions with most B motor neurons (**Fig. 1a**). What are the functions of these electrical synapses in rhythmic movement?

During forward locomotion, AVB inter-neurons exhibit elevated yet non-oscillatory neural activity [24-26]. AVB-B couplings are reminiscent of a descending pathway for motor control known in vertebrate systems. Whereas reticulospinal neurons could directly drive or modulate premotor CPGs in the spinal cord, whether similar CPG elements exist in the worm nerve cord remains unclear. Our previous work has shown that directional proprioceptive couplings between adjacent body regions are responsible for transducing and propagating rhythmic head bending activity along the worm body [27, 28]. This finding, however, did not preclude the presence of CPGs along the worm nerve cord [29].

Combining molecular genetics and optical neurophysiology for manipulating defined motor circuit components in freely behaving *C. elegans*, we found that AVB-B electrical couplings could drive a bifurcation in motor circuit dynamics, induce intrinsic oscillations in mid-body B-type motor neurons, and facilitate undulatory wave propagation. Additionally, weak electrical couplings between motor neurons allow rapid and reciprocal interaction between head and body motor activities. Our computational modeling supports that descending signals through AVB-B electrical couplings can work synergistically with proprioceptive couplings to coordinate forward locomotion in *C. elegans*.

RESULTS

AVB-B gap junctions facilitate bending wave propagation during forward locomotion

In the *C. elegans* forward motor circuit, the AVB-B electrical synapses require the expression of the UNC-7 innexin in the AVB premotor interneurons, and UNC-9 in the B motor neurons, respectively (**Fig. 1a**) [25, 30]. To determine whether AVB-B gap junctions play a role in forward locomotion, we investigated the locomotory behaviors of *unc-7* and *unc-9* mutants immersed in viscous solutions. We note that in these gap junction deficient mutants, intrinsically higher level of activity in the A-type motor neurons, which control backward locomotion, would disrupt directional forward movement [25]. To reduce the interference from the motor activity arising from the backward motor circuit, A-type motor neurons were persistently silenced by an active K^+ channel [P*unc-4*::TWK-18(gf)] in all examined strains (**Supplementary Information**).

The locomotion kinematics was visualized and quantified by curvature kymograph along the centerline of the body. During bouts of forward movement, each body segment alternates between positive (red) and negative (blue) curvature, and stripes of curvature propagate from head (head = 0) to tail (tail = 1) (**Fig. 1b**). In control animals, the bending amplitude was the highest near the head, it declined gradually and reached a plateau near the mid-body region (~ 40% worm body, **Fig. 1c**). Both *unc*-7(*hp121*) and *unc-9*(*fc16*) null mutants could propagate undulatory waves from head to tail. However, their bending amplitude diminished rapidly and monotonously towards the tail without a plateau (**Fig. 1b-d** and **Supplementary Video 1**). Similar behavioral phenotypes were observed when premotor interneurons AVB were optogenetically ablated using miniSOG [31] (P*lgc-55(B)*::miniSOG or P*sra-11*::miniSOG) (**Fig. 1b-d** and **Supplementary Fig. 1**). Rescuing innexin UNC-7 in AVB premotor interneurons (*unc*-7; P*sra-11*::UNC-7) was sufficient to restore the body bending amplitude of *unc-7* mutants (**Fig. 1c-d** and **Supplementary Video 3**).

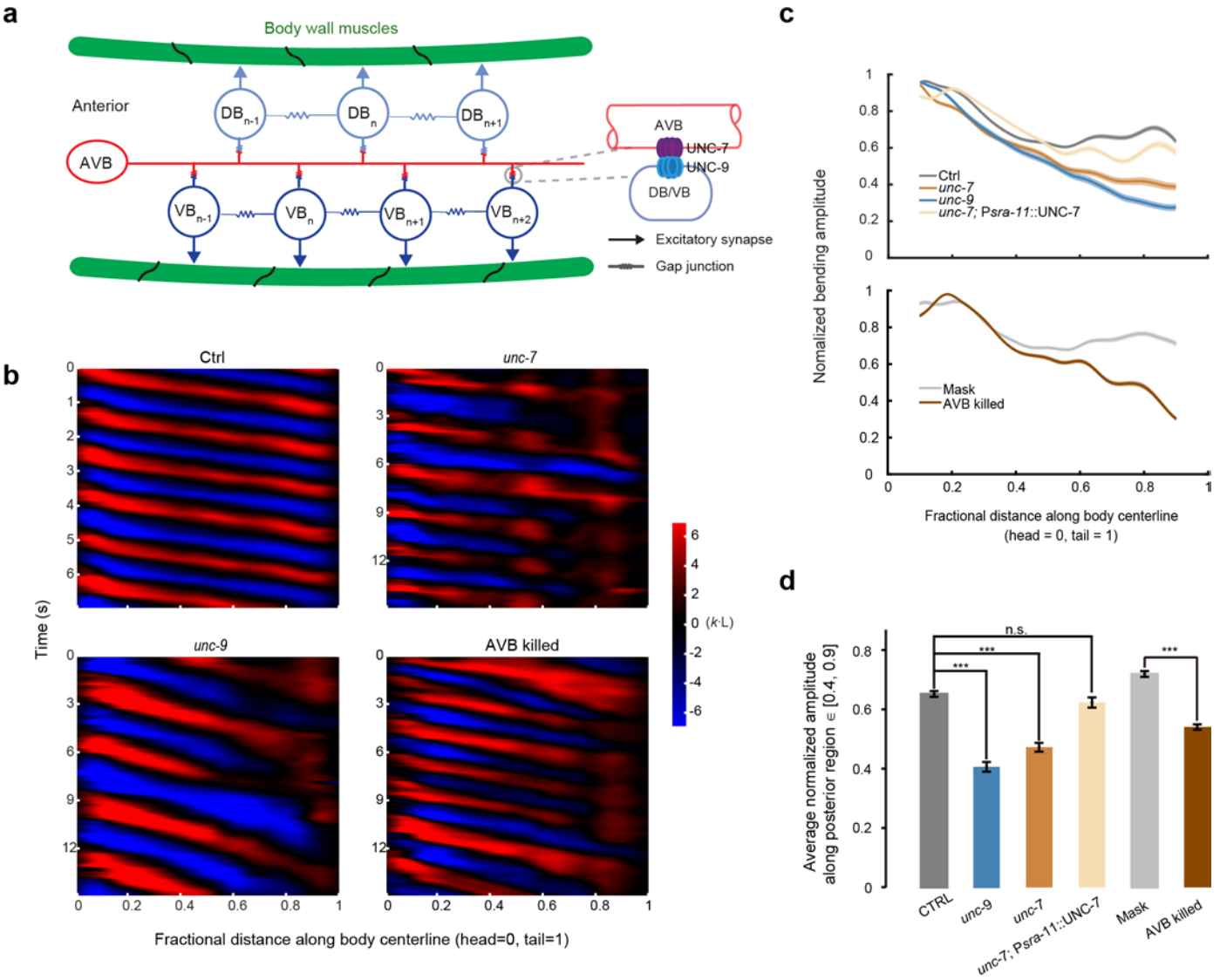

Figure 1 AVB-B electrical couplings facilitate undulatory wave propagation during forward locomotion. **(a)** A schematic diagram of gap junction highway and byway in the *C. elegans* forward motor circuit. AVB premotor interneurons form gap junctions with DB/VB motor neurons, which drive dorsal/ventral muscle contraction. The AVB-B gap junctions require the expression of innexin subunits UNC-7 in AVB and UNC-9 in B motor neurons. Neighboring B neurons are also electrically coupled. For simplicity, D-type GABAergic motor neurons are omitted in the schamatics. **(b)** Representitive curvature kymographs of control worms (N2; P*unc-4*::TWK-18(gf)), *unc-7* mutant [*unc-7*(*hp121*); P*unc-4*::TWK-18(gf)], *unc-9* mutant [*unc-9*(*fc16*); P*unc-4*::TWK-18(gf)], as well as AVB ablated worms (P*lgc*-55::miniSOG). Worms were swimming in viscous solutions (~ 1 Pa·s viscosity). Here and below, the body curvature is defined as a non-dimensional unit, $k \cdot L$, where L is the worm body length. **(c)** Comparison of bending amplitude along worm body coordinates for various strains examined above. Shaded regions represent s.e.m. The amplitude was normalized by the maximum bending curvature along the body. **(d)** Bending amplitude averaged over the posterior region $\in$ [40, 90] of the worm body. ***p<0.0001, two-sample t-test with Bonferroni correction, n.s. p = 0.16. Error bars represent s.e.m. Ctrl, n = 13 worms, 105 measurements; unc-7 mutant, n = 22 worms, 149 measurements; unc-9 mutant, n = 17 worms, 93 measurements; AVB ablated worm, n = 13 worms, 80 measurements; Mask, n =12 worms, 96 measurements.

A linear proprioceptive coupling model predicts diminished bending amplitude along the body

The coordination of body undulation during *C. elegans* forward locomotion requires proprioceptive coupling between adjacent body regions [27]. Previously, we showed that in the middle and posterior body region, curvature change induced by pneumatic microfluidic device in an anterior segment defined the curvature of the posterior neighbor, explaining the unidirectional propagation of the bending wave from from head to tail in *C. elegans* [27]. Similarly, when we trapped the middle body region of a wild type worm in a channel with defined curvature, the unrestrained posterior body region would exhibit bending curvature in the same direction as that imposed by the microfluidic channel (**Fig. 2a-b**). In *unc-7* and *unc-9* mutants, where AVB-B gap junctions are disrupted, the posterior unrestrained body region could still follow the imposed bending of the anterior body region (**Fig. 2b-c** and **Supplementary Fig. 2**), suggesting that mechanisms for proprioceptive coupling remain largely intact in these mutants.

We therefore ask why AVB-B gap junction deficient worms cannot efficiently propagate the undulatory waves. We first adopted a simple linear coupling model [27] for transducing the bending activity, in which we asserted that the undulatory wave begins with rhythmic dorsal/ventral bends near the head. Directional proprioceptive coupling between adjacent body regions is fully described by a set of first order differential equations (see **Supplementary information**). This linear coupling model, however, predicts exponential decay of bending amplitude towards the tail, independent of whether AVB and B neurons are electrically coupled (**Fig. 2d** and **Supplementary Information**). By drawing an analogy with the electrotonic length in dendritic cable theory, we define a decay length constant ξ, which, to the leading order, is given by

$$\xi \approx \frac{l}{1 - c\alpha_{max}/b},$$

subject to constraint $c\alpha_{max}/b \leq 1$. Here l is the spatial scale for proprioceptive coupling, α_{max} is the maximum muscle torque, b is the bending modulus of the worm body, and c denotes the strength of proprioceptive coupling. $\xi \to +\infty$ leads to equal bending amplitude along the worm body. Incoorporating AVB-B gap junctions into our linear model would change c to $cg_m/(g_m + g_{AVB-B})$, where g_m and g_{AVB-B} are motor neuron membrane conductance and gap junction conductance respectively. This prefactor, however, would reduce the length constant and deteriorate the propagation of bending.

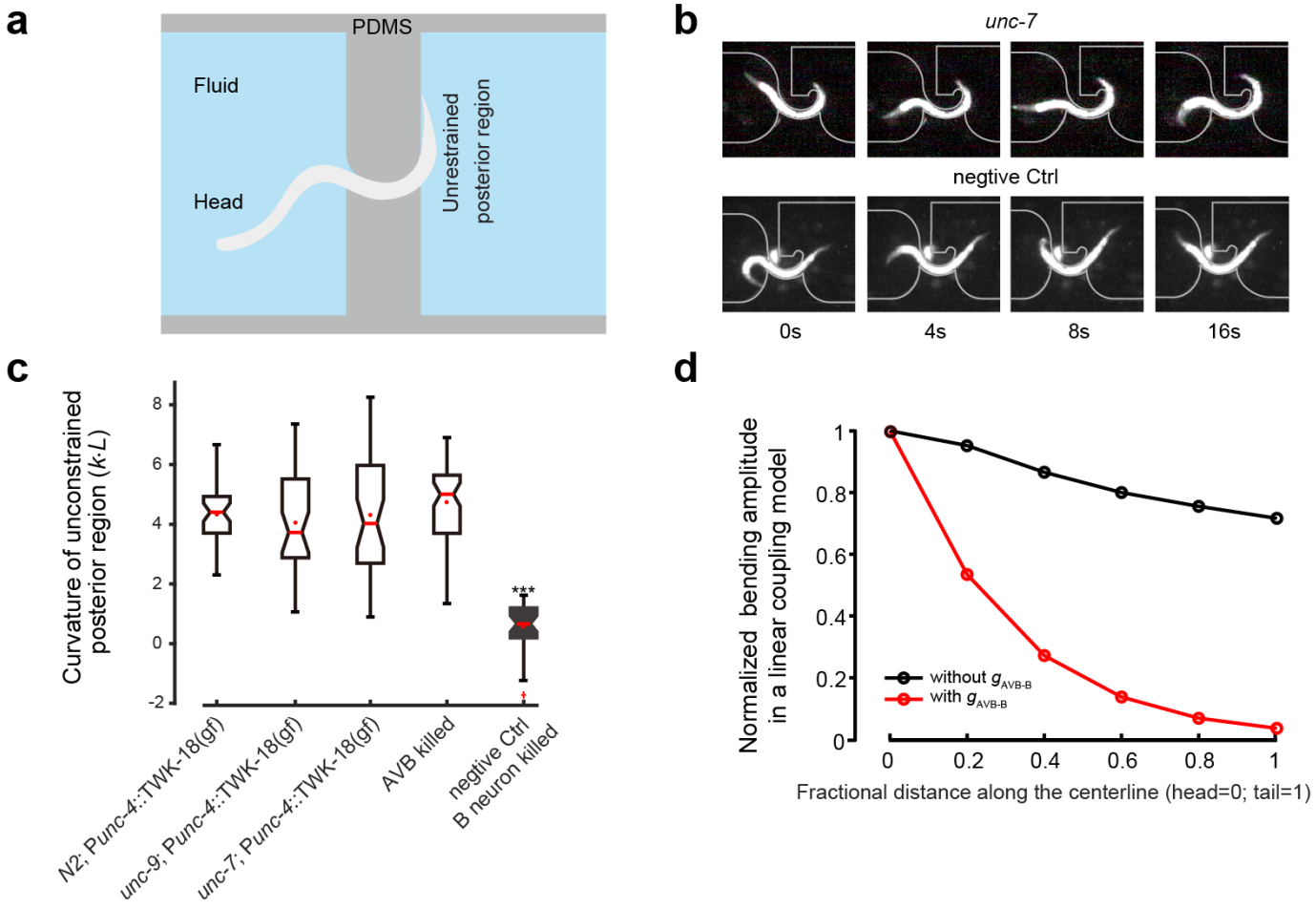

Figure 2 AVB-B electrical couplings are not necessary for transducing the proprioceptive signals. **(a)** Schematics of our microfluidic device for trapping a defined body region at a defined bending curvature. **(b)** Video images of *unc-7* and B-neuron-ablated worms trapped in our microfluidic device. **(c)** In AVB-B gap junction deficient mutants or AVB killed worms, posterior unrestrained body region could follow the curvature of the channel. However, this was not the case when B motor neurons were optogenetically ablated. Boxes indicate Q1 to Q3, error bars represent Q1-1.5IQR, Q3+1.5IQR respectively, notches indicate 95% confidential interval. *** p<0.0001, compared with all other 4 strains, Mann-Whitney U test. N2; P*unc-4*::TWK-18(*gf*), *n* = 8, 40 measurements; *unc-7*; P*unc-4*::TWK-18(gf), *n* = 12 worms, 41 measurements; *unc-9*; P*unc-4*::TWK-18(gf) mutant, *n* = 9, 38 measurements; AVB ablated worm, *n* = 10 worms, 60 measurements; negative CTRL (P*acr-5*::miniSOG), *n* = 9 worms, 33 measurements. **(d)** In our linear proprioceptive coupling model, incoorporating AVB-B gap junction inputs would deteriorate the bending wave propagation.

B motor neurons are nonlinear functional units

The discrepancy between theory and experimental observations suggests that some basic assumption in the linear model must be modified. We hypothesize that proprioceptive signal is used to couple *nonlinear* functional units within adjacent body regions, a computational ingredient that is reminiscent of incorporating voltage-dependent conductance along passive dendritic branches. In one scenario, the nonlinear functional units are intrinsic oscillators, and we set out to test whether CPGs exist along the worm nerve cord.

Our linear coupling model predicts that abolishing head bending activity would completely abolish the undulatory wave; a coupled CPGs model predicts the opposite. To distinguish these possibilities, we performed spatially selective optogenetic inhibition of B motor neurons in a defined anterior body region (**Fig. 3a-b** and **Supplementary Video 2**) of freely swimming transgenic worms (P*acr-5*::Arch). Bending activity near the head was abolished during green light illumination (**Fig. 3b, curvature kymograph**). Interestingly, higher frequency and lower amplitude undulation emerged from the mid-body (~50% body length) (**Fig. 3b, 3e**). We observed similar phenomena in a different transgenic strain expressing archaerhodopsin in both B and A motor neurons (P*acr-2(s)*::Arch, **Supplementary Fig. 3a**), or by inhibiting head muscle cells (P*myo-3*::NpHR, **Supplementary Fig. 3a**).

These observations suggest that the mid-body motor neurons could generate high frequency oscillations. The *C. elegans* premotor interneurons (AVA, AVB) do not exhibit rhythmic activity correlated with body bending [25]. Moreover, while the undulation frequency decreased in more viscous solution [32], the frequency of light-induced mid-body undulation remained fixed across a wide range of viscosities (**Fig. 3c** and **Supplementary Fig. 3b**). The lack of dependence of mid-body undulation frequency on the mechanical load indicates that rhythmic activity might be generated cell-autonomously.

To determine whether B motor neurons generate mid-body oscillation when head and body were decoupled, we performed systematic optogenetic ablation of B motor neurons (P*acr-5*::miniSOG) localized in worm ventral nerve cord. Ablating a subgroup of mid-body B motor neurons (DB4-5 and VB5-7) completely abolished optogenetically-induced fast oscillation (**Fig. 3d-e**). When fewer B neurons in this cluster were ablated, fast mid-body undulation could still be induced (**Supplementary Fig. 3**). Sometimes, we even observed two decoupled waves emerged from head and posterior body regions (**Supplementary Fig. 3**c). Together, these data strongly suggest that the motor circuit in certain body region is not simply responding to the proprioceptive signal from an anterior body region. B motor neurons are thus nonlinear functional units and constitute distributed CPG modules along the body.

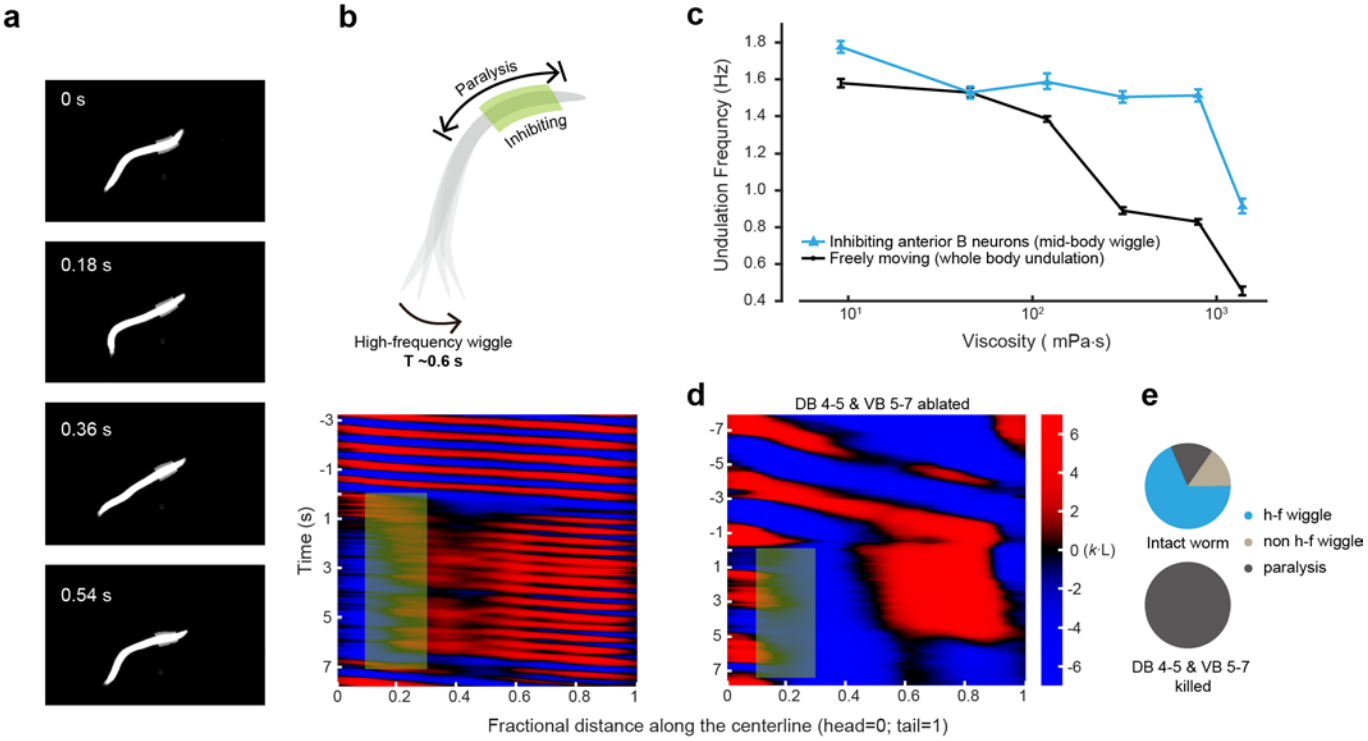

Figure 3 Mid-body B motor neurons could intrinsically generate rhythmic activity. **(a)** Video images of a head-body-decoupled worm, when B motor neurons in the anterior body region (0.1-0.3 fractional distance along body coordinate) were optogenetically inhibited. **(b)** Up, schematic shows spatially selective inhibition of B motor neurons in an anterior body region induced high-frequency wiggling in the posterior region; bottom, curvature kymograph of a representative experiment. Green-shaded region shows the spatiotemporal selected region for optogenetic inhibition. **(c)** Undulation frequency with the medium viscosity. Black, normal swimming worm; blue, mid-body undulation when head and body were decoupled. Error bars are s.e.m. for each data point with $n \geq 8$ worms. **(d)** Representative curvature kymograph during spatially selective optogenetic inhibition of anterior B motor neurons and after mid-body B neurons (DB 4-5 & VB 5-7) were optogenetically ablated. **(e)** The pie chart summarizes worm locomotor states across trials when head and body were decoupled. h-f wiggle: mid-body undulation frequency was higher than that before head and body were decoupled; non h-f wiggle: mid-body undulation frequency is equal to or less than that before head and body were decoupled; paralysis: no waves emerged. Intact worms (P*acr-5*::Arch), n = 20 worms, 241 measurements. Mid-body B neurons ablated worms (P*acr-5*::Arch; P*acr-5*::miniSOG), n =11 worms, 77 measurements.

AVB-B gap junctions drive a bifurcation in B neuron dynamics

We next ask whether AVB-B gap junction inputs participate in driving fast mid-body oscillation when head and body were decoupled. Indeed, in AVB-B gap junction deficient mutants, or AVB ablated worms, optogenetically-induced mid-body fast undulation was almost completely abolished (**Fig. 4a-b**). Inhibiting anterior B motor neurons, or inhibiting anterior body wall muscles, which eliminated head bending activity and thereby the proprioceptive signal, would cause whole-body paralysis (**Fig. 4a-b** and **Supplementary Fig. 4**). Rescuing innexin subunits UNC-7 in AVB (*unc*-7; P*sra-11*::UNC-7) significantly restored the light-induced fast undulation (**Fig. 4b** and **Supplementary Video 3**).

From a dynamic systems point of view, our data suggest that AVB-B gap junction inputs could drive a bifurcation in B neuron dynamics, leading to a transition from being stationary to rhythmic oscillation. In the presence of AVB-B gap junction inputs, the dynamics of B motor neuron loses its stability. Time-varying proprioceptive signal from anterior body region may easily trigger large change in motor neuron membrane potential and thus facilitate bending wave propagation.

This intuition was recapitulated by our simulation of a nonlinear coupling model (**Supplementary Information**), modified to incorporate the following two experimental observations. First, without a strong proprioceptive signal, AVB-B electrical couplings could induce high frequency rhythmic bending activity, driven by B motor neurons. Second, proprioceptive signals could entrain B motor neurons to oscillate at a normal (slower) undulation frequency. Our simulation shows that, indeed, AVB-B gap junction inputs could help equalize the bending amplitude along the body (**Fig. 1b, 4c**).

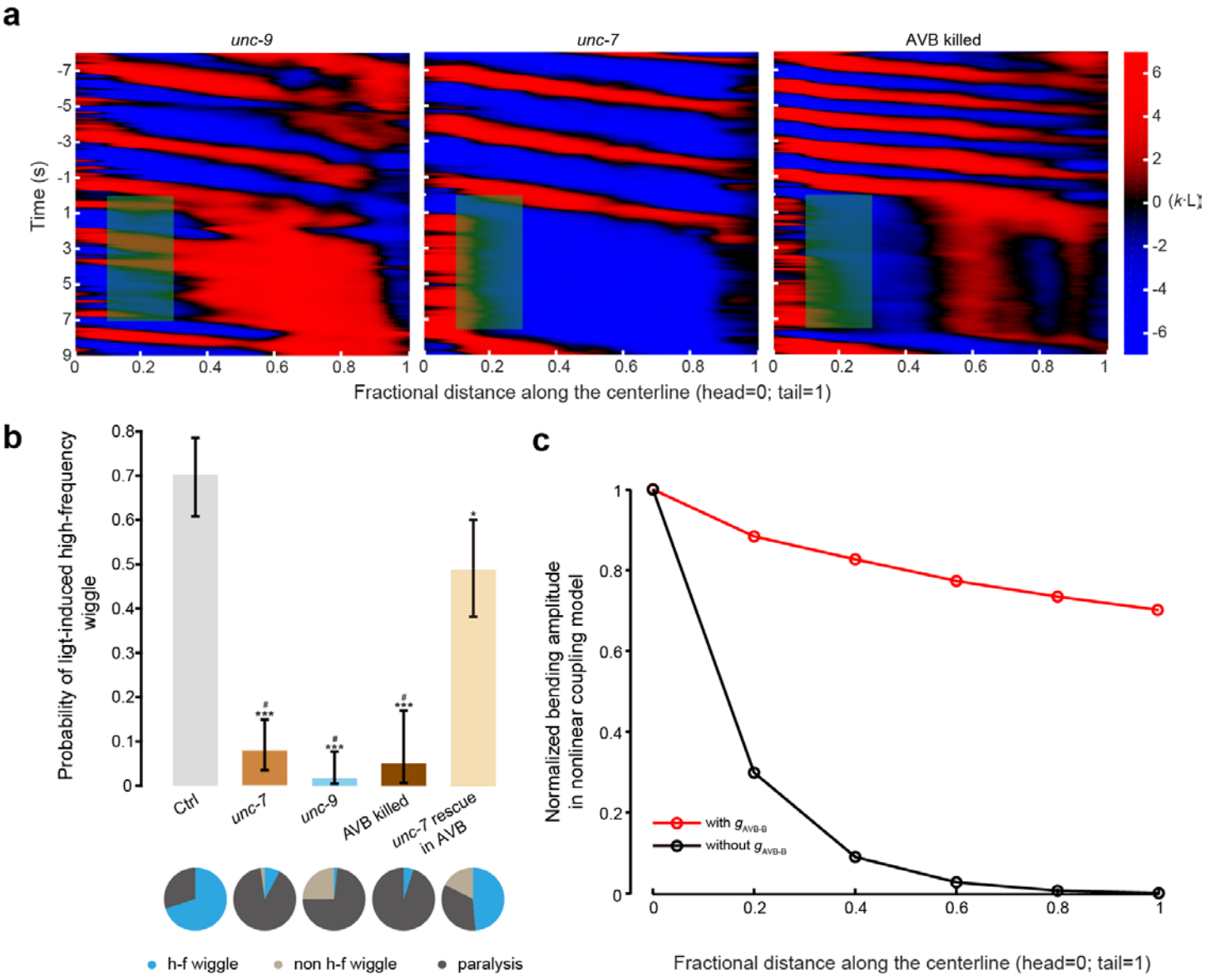

Figure 4 AVB-B electrical couplings drive a bifurcation in B neuron dynamics. **(a)** Representative curvature kymographs of head-body-decoupled experiments in AVB-B gap junction deficient or AVB ablated worms. **(b)** The probability for inducing high frequency mid-body undulation when head and body were decoupled. The pie chart summarizes the worm locomotor states. Error bars indicate 95% binomial proportion confidence interval. ***p < 0.0001, *p=0.002, # p < 0.0001, (* compared with Ctrl, # compared with UNC-7 rescued in AVB) Chi-square test. Strains for comparisions are: control worm [P*acr-5*::Arch; P*unc-4*::TWK-18(gf)], *n* = 13 worms, 113 measurements; *unc-7* [*unc-7*(*hp121*); P*acr-5*::Arch; P*unc-4*::TWK-18(gf)] *n* = 21 worms, 102 measurements; *unc-9* [*unc-9*(*fc16*); P*acr-5*::Arch; P*unc-4*::TWK-18(gf)] *n* = 26 worms, 116 measurements; AVB ablated [P*lgc-55(B)*::miniSOG, P*acr-5*::Arch] *n* = 11 worms, 40 measurements; UNC-7 rescued in AVB [*unc-7*(*hp121*); P*acr-5*::Arch; P*unc-4*::TWK-18(gf); P*sra-11*::UNC-7] *n* = 12 worms, 86 measurements. **(c)** Comparison of the normalized bending amplitude with and without AVB-B gap junction in our nonlinear proprioceptive coupling model.

Electrical couplings between motor neurons allow rapid and reciprocal interactions between head and body motor activities

Having considered the functions of AVB-B gap junctions, we next ask whether local gap junctions between motor neurons (**Fig. 1a**), identified by the anatomical wiring diagram [22, 23], play a role in controlling worm locomotion. Interestingly, spatially selective optogenetic inhibition of B motor neurons localized in the middle or posterior body region of a freely swimming worm could reliably induce whole body paralysis within ~ 300 ms (**Fig. 5a-b**, **Supplementary Fig. 5** and **Supplementary Video 4**). Electrical coupling is the best candidate for rapid redistribution of a hyperpolarization current in B motor neurons (P*acr-5*::Arch). We found that in either *unc-7* mutants or AVB ablated worms, whole body paralysis could still be induced (**Fig. 5c**), suggesting that in the absence of AVB-B gap junctions, the hyperpolarization signal could still be transduced. However, in *unc-9* mutants, rhythmic bending activity in the anterior body region persisted when mid-body B motor neuron were silenced (**Fig. 5a, 5c** and **Supplementary Video 5**), and rescuing UNC-9 expression in B and A motor neurons (P*acr-2*::UNC-9) was sufficient to restore light-induced whole body paralysis (**Fig. 5c**). These results suggest that electrical couplings between motor neurons contribute to the paralytic effect.

The probability of light-induced whole-body paralysis was dose-dependent. Lower laser intensity, which reduced the degree of hyperpolarization in mid-body B motor neurons, did not abolish forward movement, but reduced the frequency and amplitude of whole body undulation (**Fig. 5d-e**). Together, these data suggest that electrical couplings between motor neurons may retrogradely regulate the head bending activity, hence reconfiguring the dynamics of the body undulation.

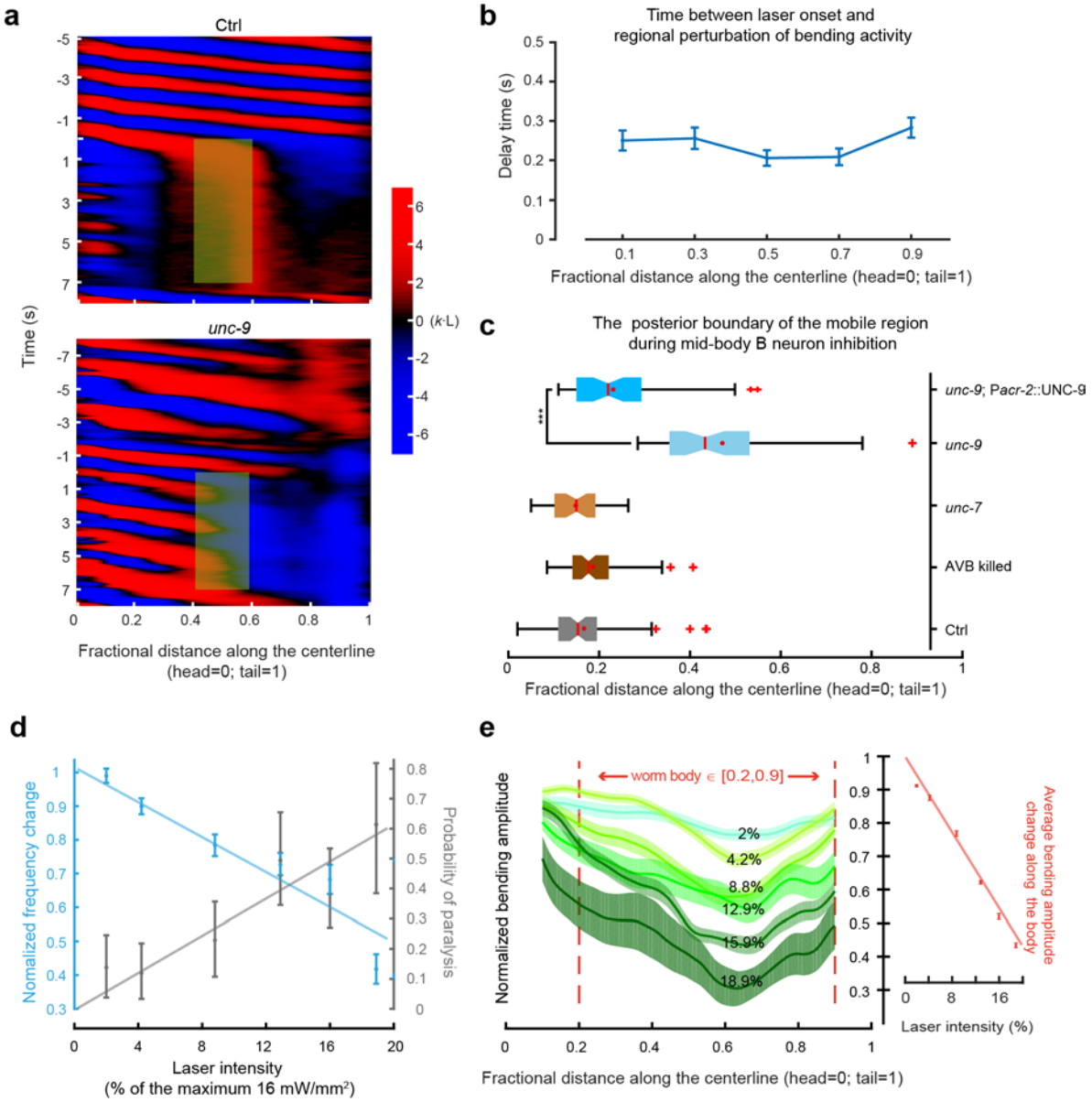

Figure 5 Electrical couplings between motor neurons allow rapid and reciprocal interactions between head and body motor activities. **(a)** Comparison of representative curvature kymographs of a control worm [P*acr-5*::Arch; P*unc-4*::TWK-18(gf)] and an *unc-9* mutant [*unc-9*(*fc16*); P*acr-5*::Arch; P*unc-4*::TWK-18(gf)] during optogenetic inhibition of mid-body B motor neurons. Green shaded regions are spatiotemporal selected region (0.4-0.6 fractional distance along worm body, 0-7 seconds) for optogenetic manipulation. **(b)** Delay time between green laser onset and a detectable perturbation in regional bending activity. Error bars are s.e.m. We measured the delay time by first fitting undulatory wave with sinusoidal function before mid-B neuron inhibition and by a linear fit of curvature during mid-B neuron inhibition. The crossover point stands for the wiggling-to-paralysis transition (**Supplementary Fig. 5**). **(c)** Quantification of the immobilization effect during optogenetic inhibition of mid-body B motor neurons. Red crosses are outliers. Red lines are mediums, red dots are mean, error bars represent Q1-1.5IQR, Q3+1.5IQR respectively, and notches indicate 95% confidential interval. In *unc-9* mutants, the boundary shifted towards the mid-body, suggesting that the entire anterior body region could still wiggle. *** p<0.0001, Mann-Whitney U test. Strains for comparisions are: control worm [P*acr-5*::Arch; P*unc-4*::TWK-18(gf)], *n* = 17 worms, 70 measurements; *unc-7* [*unc-7*(*hp121*); P*acr-5*::Arch; P*unc-4*::TWK-18(gf)] *n* = 11 worms, 43 measurements; *unc-9* [*unc-9*(*fc16*); P*acr-*

5::Arch; P*unc-4*::TWK-18(gf)] *n* = 17 worms, 59 measurements; AVB ablated (P*lgc-55*::miniSOG, P*acr-5*::Arch) *n* = 18 worms, 65 measurements; UNC-9 rescued in B and A motor neurons [*unc-9*(*fc16*); P*acr-5*::Arch; P*acr-2s*::UNC-9] *n* = 9 worms, 48 measurements. **(d)** Dose (laser intensity) dependent effect on undulation frequency and on the efficacy for inducing whole-body paralysis. Error bars (blue), s.e.m. error bars (gray), 95% binomial proportion confidence interval. $n \geq 5$ worms for each data point. Maxmium intensity: 16 mW/mm^2 . Line is a linear regression fit, $R^2 = 0.899$ (blue), $R^2 = 0.878$ (gray). **(e)** Dose dependent effect on bending amplitude along the worm body. Line is a linear regression fit $R^2 = 0.986$. Error bars are s.e.m. Maxmium intensity: 16 mW/mm^2

DISCUSSION

In vertebrate motor systems, global descending signals from the hindbrain can drive premotor CPG networks in the spinal cord to generate rhythmic motor patterns [10]. In *C. elegans*, we discovered that the B class motor neurons themselves are not passive recipients of descending command neuron inputs. Instead, AVB-B electrical couplings could induce intrinsic oscillations in at least some B motor neurons (**Fig. 6b**), and facilitate undulatory wave propagation. *C. elegans*, due to the cellular economy of its nervous system, has implemented a compressed yet converging algorithm for motor control.

We have developed a phenomenological nonlinear coupling model to explain our experimental observations (**Supplementary Information**). In the model, we divided whole worm into several segments, and the segment number is accordance with the number of DB motor neurons. The excitatory motor neurons were modeled as nonlinear functional units with active voltage gated ion channels. Because the detailed form of intrinsic membrane conductance in B motor neurons remains unknown, we have used the classic phenomenological model based on persistent Ca^{2+} and K^{+} conductances, which suffice to account for key experimental findings. Although a class of nonlinear neuron models could generate intrinsic rhythmic activity [33], distinguishing them requires electrophysiological recording in tiny worm motor neurons, an extremely difficult technique that has just recently become possible [34]. Intriguingly, a complementary study has found that voltage dependent Ca^{2+} channels are required for generating intrinsic rhythmic activity in A-type motor neurons (personal communication with Shangbang Gao and Mei Zhen). Whether similar channels drive the B-type motor neuron oscillations may be addressed in future studies.

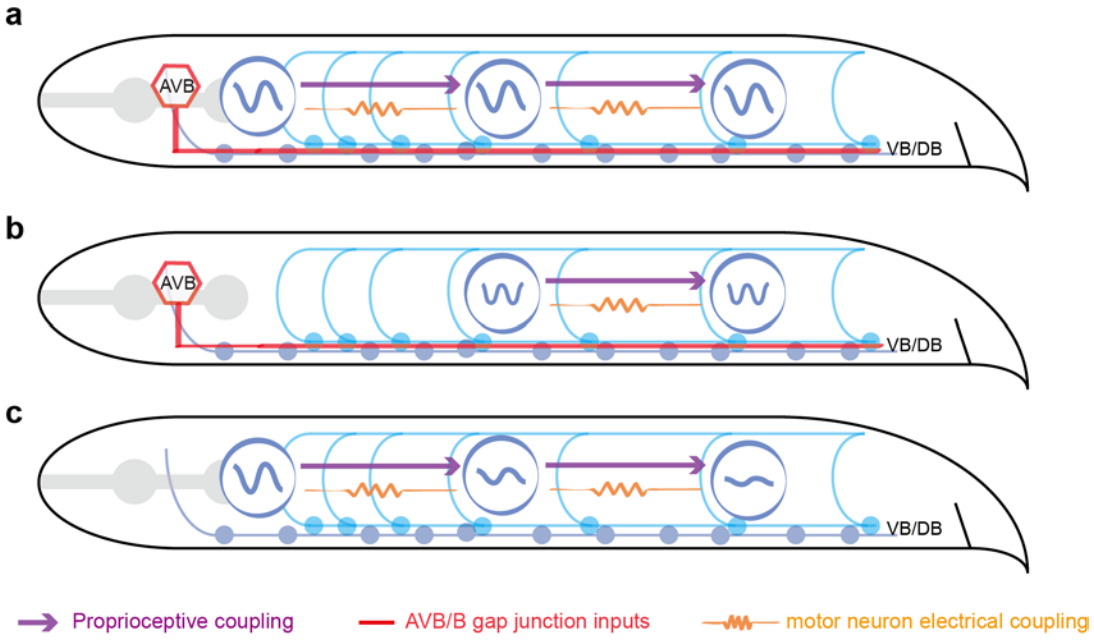

Figure 6 Model schematics of coordinating forward locomotion in *C. elegans*. **(a)** Proprioceptive coupling, AVB-B gap junction inputs and weak electrical couplings between B neurons work synergistically to drive and propagate a well-formed undulatory wave from head to tail. **(b)** Without a strong and time-varying proprioceptive signal from an anterior body region, AVB-B gap junction inputs could induce mid-body high frequency undulation. **(c)** Without AVB-B gap junction inputs, proprioceptive couplings are less effective in propagating the bending waves, leading to diminished bending amplitude towards the tail.

We also found a previously unknown role of electrical coupling between motor neurons, which would allow rapid and reciprocal interaction between head and body motor activities (**Fig. 5-6**). Strong electrical coupling between motor neurons would tend to synchronize motor activity along the whole worm body and thus deteriorate bending wave propagation (over-expressing UNC-9 in B motor neurons would paralyze worms, **Supplementary Video 6**). During normal locomotion, weak electrical couplings between motor neurons might help mediate the undulation frequency along the whole worm and augment the excitability of motor neurons. Consistent with this view, we found that optogenetically ablating mid-body B neurons reduced the head undulation frequency (**Supplementary Fig. 1a** and **Supplementary Fig. 3d**). Direct test of the functional contribution of local electrical couplings would require eliminating electrical synapses between motor neurons, while sparing the AVB-B ones. However, current genetic tools for manipulating gap junction expression with defined wiring specificity remain to be developed because both types of gap junctions require UNC-9 innexin subunits.

UNC-9 is also express in *C. elegans* body wall muscle cells [35]. Could electrical coupling between muscle cells and electrical coupling between motor neurons have similar functions? We and others found that spatially selective optogenetic inhibition of mid-body muscle cells did not affect the bending activity in the anterior body

region, but would abolish the bending activity in the posterior body region [36], consistent with our proprioceptive coupling model (**Fig. 6**). Furthermore, in *unc-13* mutants, which lack motor neuron inputs, optogenetically activating targeted ventral or dorsal muscle cells could induce local body bending, but did not induce bending in neighboring regions [27]. These data suggest that electrical coupling between body wall muscle cells may play a more localized role in mediating the bending activity in *C. elegans*.

The functional implication of gap junction in the context of neural circuit and behavior could be counterintuitive, confounding and are often underestimated [37, 38]. Insight has been gained from studying small nervous systems, where individual neurons can be identified and connectivity between neurons could be mapped out. Experimental and modeling studies on crustacean stomatogastric ganglion suggested that the strength of electrical synapses can mediate the frequency of coupled oscillators [39]; the interplay between electrical and chemical synapses provides degenerate circuit mechanisms for switching between fast and slow oscillatory behaviors [40]. In *C. elegans,* electrical synapse could offer a parallel pathway for routing sensory information [41, 42], or participate in coincident detection of multiple sensory cues [43]. Our findings also demonstrate that electrical couplings can have a potent influence on the motor circuit dynamics.

Our data suggest that *distributed* CPGs exist in the *C. elegans* ventral nerve cord. Because worm must adapt extreme ranges of external mechanical load imposed by a changing environment [32], directional proprioceptive couplings transduced by B motor neurons [27] play the pivotal role in entraining the rhythm of body oscillators and in propagating coherent bending waves from head to tail (**Fig. 6**). Despite substantial difference between worm motor circuit and those in higher animals, the neural computation for coordinating *C. elegans* locomotion could now also be categorized into a coupled CPG model (**Fig. 6**). The building blocks for CPG and the detailed coupling mechanisms between CPGs could vary across species [5, 6], yet the overarching principles underlying body coordination appear to be surprisingly similar. By integrating neuromuscular dynamics and biomechanical feedback, our findings represent one step towards a full systems model of animal locomotion.

METHODS

Worm Strains and Cultivation

Wild-type (N2), mutant, and transgenic worms were cultivated using standard methods [44]. Strain information can be found in the Supplementary Experimental Procedures. Transgenic worms used in all optogenetic experiments were cultivated in dark at 20-25ºC on NGM plates with *Escherichia coli* OP50 and all-*trans* retinal (ATR). We performed all experiments using young adult hermaphrodites.

Microfluidic Devices

Custom microfluidic devices were fabricated in PDMS using soft lithography techniques. We loaded each microfluidic channel with dextran solution [~25% dextran in M9 buffer (1 Pa·s viscosity)]. An individual worm was flowed into the inlet of each microfluidic channel and worm position within each channel was manually controlled by syringes connected to polyethylene tubing.

Behavioral Quantification and Optogenetic Manipulation

Experiments were performed on a Nikon inverted microscope (Ti-U) under 10X magnification with dark field illumination. Worms were immersed in viscous solution (~25% dextran in M9 buffer in most cases), sandwiched between two glass slides, and were retained within the field of view of an imaging objective by a custom tracking system. Video sequences were taken by a Basler CMOS camera (aca2000-340km), and worm body centerline were extracted in real-time. We used custom software written in MATLAB (MathWorks, Inc. Natick, MA) for post-processing the behavioral data. We used CoLBeRT system [36] to perform spatially-selective optogenetic manipulation for different motor circuit components. For optogenetic inhibition, we used a 561 nm solid-state laser with maximum intensity at 16 mW/mm^2.

Optogenetic Ablation

Optogenetic ablation was carried out on transgenic strains in which mitochondrially targeted miniSOG (mini singlet oxygen generator) was specifically expressed in *C. elegans* neurons. Upon blue light illumination, mito-miniSOG causes rapid cell death in a cell-autonomous manner [31]. To ablate AVB neurons [*Plgc*-55(B)::miniSOG or *Psra-11*::miniSOG], L3/early L4 worms cultivated on OP50 were transplanted to an unseeded NGM plate, restricted within ~1.7 cm^2 area via filter paper with a hole in the center and soaked with 100 μM $CUCL_2$. Worms were illuminated with blue LED light (M470L3-C5, Thorlabs, Inc.) with intensity 80.2 mW/cm^2, measured by power meter (PM16-130, Thorlabs, Inc.). The temporal sequence was 0.5/1.5 s on/off pulses for 30 min. After illumination, worms were transplanted to newly OP50 seeded NGM plate with/without ATR for latter behavioral experiments.

For selective B motor neuron ablation (*Pacr-5*::miniSOG), single L3/early L4 worm was picked up from OP50 seeded NGM plate to a 3% agarose (wt/vol) coated glass slide. Worm was covered by a cover glass to be kept stationary. Spatially selective illumination pattern was generated by a digital micromirror device (DLI4130 0.7 XGA, Digital Light Innovations, Texas) to target individual neurons through a 20X objective mounted on a Nikon inverted microscope (Ti-U). Neurons were identified using mCherry fluorescence signal. We used 473 nm blue laser with intensity 29 mW/mm^2. The temporal sequence was 0.5/1.5 s on/off pulses for 15 min. After illumination, the worm was first recovered by 2 μl M9 buffer, and was transplanted to OP50 seeded NGM plated with/without ATR for latter behavioral experiment.

AUTHOR CONTRIBUTIONS

T.X. and Q.W. conceived the project. T.X. and J.H. performed all experiments. T.X. performed all data analysis. S.S. and Q.W. developed the computational model. J.H., M.P., T.K., Y.L., M.W. made all reagents and transgenetic lines used in this work. Q.W. wrote the manuscript with inputs from M.Z., T.X. and S.S.

ACKNOWLEDGMENTS

The authors thank Christopher Fang-Yen and Anthony Fouad for helpful discussion. This work was funded by the CAS Hundreds Talents Plan and National Science Foundation of China (NSFC-31471051 and NSFC-91632102).

REFERENCES

1. Brown, T.G. The Intrinsic Factors in the Act of Progression in the Mammal. *Proceedings of the Royal Society of London Series B-Biological Sciences* **84**, 308-319 (1911).
2. Delcomyn, F. Neural basis of rhythmic behavior in animals. *Science* **210**, 492-498 (1980).
3. Grillner, S. The motor infrastructure: from ion channels to neuronal networks. *Nat Rev Neurosci* **4**, 573-586 (2003).
4. Kiehn, O. Locomotor circuits in the mammalian spinal cord. *Annu Rev Neurosci* **29**, 279-306 (2006).
5. Marder, E., Bucher, D., Schulz, D.J. & Taylor, A.L. Invertebrate central pattern generation moves along. *Curr Biol* **15**, R685-699 (2005).
6. Marder, E. & Calabrese, R.L. Principles of rhythmic motor pattern generation. *Physiological Reviews* **76**, 687-717 (1996).
7. Mullins, O.J., Hackett, J.T., Buchanan, J.T. & Friesen, W.O. Neuronal control of swimming behavior: comparison of vertebrate and invertebrate model systems. *Prog Neurobiol* **93**, 244-269 (2011).
8. Kiehn, O. Decoding the organization of spinal circuits that control locomotion. *Nat Rev Neurosci* **17**, 224-238 (2016).
9. Goulding, M. Circuits controlling vertebrate locomotion: moving in a new direction. *Nat Rev Neurosci* **10**, 507-518 (2009).
10. Lemon, R.N. Descending pathways in motor control. *Annu Rev Neurosci* **31**, 195-218 (2008).
11. Hagglund, M., Borgius, L., Dougherty, K.J. & Kiehn, O. Activation of groups of excitatory neurons in the mammalian spinal cord or hindbrain evokes locomotion. *Nat Neurosci* **13**, 246-252 (2010).
12. Thiele, T.R., Donovan, J.C. & Baier, H. Descending control of swim posture by a midbrain nucleus in zebrafish. *Neuron* **83**, 679-691 (2014).
13. Severi, K.E.*, et al.* Neural control and modulation of swimming speed in the larval zebrafish. *Neuron* **83**, 692-707 (2014).
14. Bouvier, J.*, et al.* Descending Command Neurons in the Brainstem that Halt Locomotion. *Cell* **163**, 1191-1203 (2015).
15. Esposito, M.S., Capelli, P. & Arber, S. Brainstem nucleus MdV mediates skilled forelimb motor tasks. *Nature* **508**, 351-356 (2014).
16. Connors, B.W. & Long, M.A. Electrical synapses in the mammalian brain. *Annu Rev Neurosci* **27**, 393-418 (2004).
17. Kiehn, O. & Tresch, M.C. Gap junctions and motor behavior. *Trends Neurosci* **25**, 108-115 (2002).
18. Szczupak, L. Functional contributions of electrical synapses in sensory and motor networks. *Curr Opin Neurobiol* **41**, 99-105 (2016).
19. Tresch, M.C. & Kiehn, O. Motor coordination without action potentials in the mammalian spinal cord. *Nat Neurosci* **3**, 593-599 (2000).
20. Song, J., Ampatzis, K., Bjornfors, E.R. & El Manira, A. Motor neurons control locomotor circuit function retrogradely via gap junctions. *Nature* **529**, 399-402 (2016).
21. White, J.G., Southgate, E., Thomson, J.N. & Brenner, S. The structure of the ventral nerve cord of Caenorhabditis elegans. *Philos Trans R Soc Lond B Biol Sci* **275**, 327-348 (1976).
22. White, J.G., Southgate, E., Thomson, J.N. & Brenner, S. The structure of the nervous system of the nematode Caenorhabditis elegans. *Philos Trans R Soc Lond B Biol Sci* **314**, 1-340 (1986).
23. Chen, B.L. Neuronal Network of C. elegans: from Anatomy to Behavior. in *The Watson School of Biological Sciences* 96 (Cold Spring Harbor Laboratory, Cold Spring Harbor 2007).
24. Faumont, S.*, et al.* An image-free opto-mechanical system for creating virtual environments and imaging neuronal activity in freely moving Caenorhabditis elegans. *PLoS One* **6**, e24666 (2011).
25. Kawano, T.*, et al.* An Imbalancing Act: Gap Junctions Reduce the Backward Motor Circuit Activity to Bias C. elegans for Forward Locomotion. *Neuron* **72**, 572-586 (2011).
26. Laurent, P.*, et al.* Decoding a neural circuit controlling global animal state in C. elegans. *Elife* **4** (2015).

27. Wen, Q.*, et al.* Proprioceptive coupling within motor neurons drives C. elegans forward locomotion. *Neuron* **76**, 750-761 (2012).
28. Zhen, M. & Samuel, A.D. C. elegans locomotion: small circuits, complex functions. *Curr Opin Neurobiol* **33**, 117-126 (2015).
29. Gjorgjieva, J., Biron, D. & Haspel, G. Neurobiology of Caenorhabditis elegans Locomotion: Where Do We Stand? *Bioscience* **64**, 476-486 (2014).
30. Starich, T.A., Xu, J., Skerrett, I.M., Nicholson, B.J. & Shaw, J.E. Interactions between innexins UNC-7 and UNC-9 mediate electrical synapse specificity in the Caenorhabditis elegans locomotory nervous system. *Neural Dev* **4** (2009).
31. Qi, Y.B., Garren, E.J., Shu, X., Tsien, R.Y. & Jin, Y. Photo-inducible cell ablation in Caenorhabditis elegans using the genetically encoded singlet oxygen generating protein miniSOG. *Proc Natl Acad Sci U S A* **109**, 7499-7504 (2012).
32. Fang-Yen, C.*, et al.* Biomechanical analysis of gait adaptation in the nematode Caenorhabditis elegans. *Proc Natl Acad Sci U S A* **107**, 20323-20328 (2010).
33. Izhikevich, E.M. *Dynamical systems in neuroscience : the geometry of excitability and bursting* (MIT Press, Cambridge, Mass., 2007).
34. Liu, P., Chen, B., Mailler, R. & Wang, Z.W. Antidromic-rectifying gap junctions amplify chemical transmission at functionally mixed electrical-chemical synapses. *Nat Commun* **8**, 14818 (2017).
35. Liu, Q., Chen, B., Gaier, E., Joshi, J. & Wang, Z.W. Low conductance gap junctions mediate specific electrical coupling in body-wall muscle cells of Caenorhabditis elegans. *J Biol Chem* **281**, 7881-7889 (2006).
36. Leifer, A.M., Fang-Yen, C., Gershow, M., Alkema, M.J. & Samuel, A.D. Optogenetic manipulation of neural activity in freely moving Caenorhabditis elegans. *Nature Methods* **in press** (2011).
37. Manor, Y., Rinzel, J., Segev, I. & Yarom, Y. Low-amplitude oscillations in the inferior olive: a model based on electrical coupling of neurons with heterogeneous channel densities. *J Neurophysiol* **77**, 2736-2752 (1997).
38. Marder, E. Electrical synapses: beyond speed and synchrony to computation. *Curr Biol* **8**, R795-797 (1998).
39. Kepler, T.B., Marder, E. & Abbott, L.F. The effect of electrical coupling on the frequency of model neuronal oscillators. *Science* **248**, 83-85 (1990).
40. Gutierrez, G.J., O'Leary, T. & Marder, E. Multiple mechanisms switch an electrically coupled, synaptically inhibited neuron between competing rhythmic oscillators. *Neuron* **77**, 845-858 (2013).
41. Jang, H.*, et al.* Dissection of neuronal gap junction circuits that regulate social behavior in Caenorhabditis elegans. *Proc Natl Acad Sci U S A* **114**, E1263-E1272 (2017).
42. Macosko, E.Z.*, et al.* A hub-and-spoke circuit drives pheromone attraction and social behaviour in C. elegans. *Nature* **458**, 1171-1175 (2009).
43. Rabinowitch, I., Chatzigeorgiou, M. & Schafer, W.R. A gap junction circuit enhances processing of coincident mechanosensory inputs. *Curr Biol* **23**, 963-967 (2013).
44. Brenner, S. The genetics of Caenorhabditis elegans. *Genetics* **77**, 71-94 (1974).

Supplementary Information

A descending pathway through electrical coupling facilitates undulatory wave propagation in *C. elegans*

Tianqi Xu[1,3], Jing Huo[1,3], Shuai Shao[1], Min Wu[2], Michelle Po[2], Taizo Kawano[2], Yangning Lu[2], Mei Zhen[2], Quan Wen[1,*]

1. Chinese Academy of Sciences Key Laboratory of Brain Function and Disease, School of Life Sciences, University of Science and Technology of China, Hefei, China

2. Lunenfeld-Tanenbaum Research Institute, Mount Sinai Hospital, University of Toronto, Toronto, ON, Canada

3. These authors contribute equally to this work

*Corresponding author: qwen@ustc.edu.cn

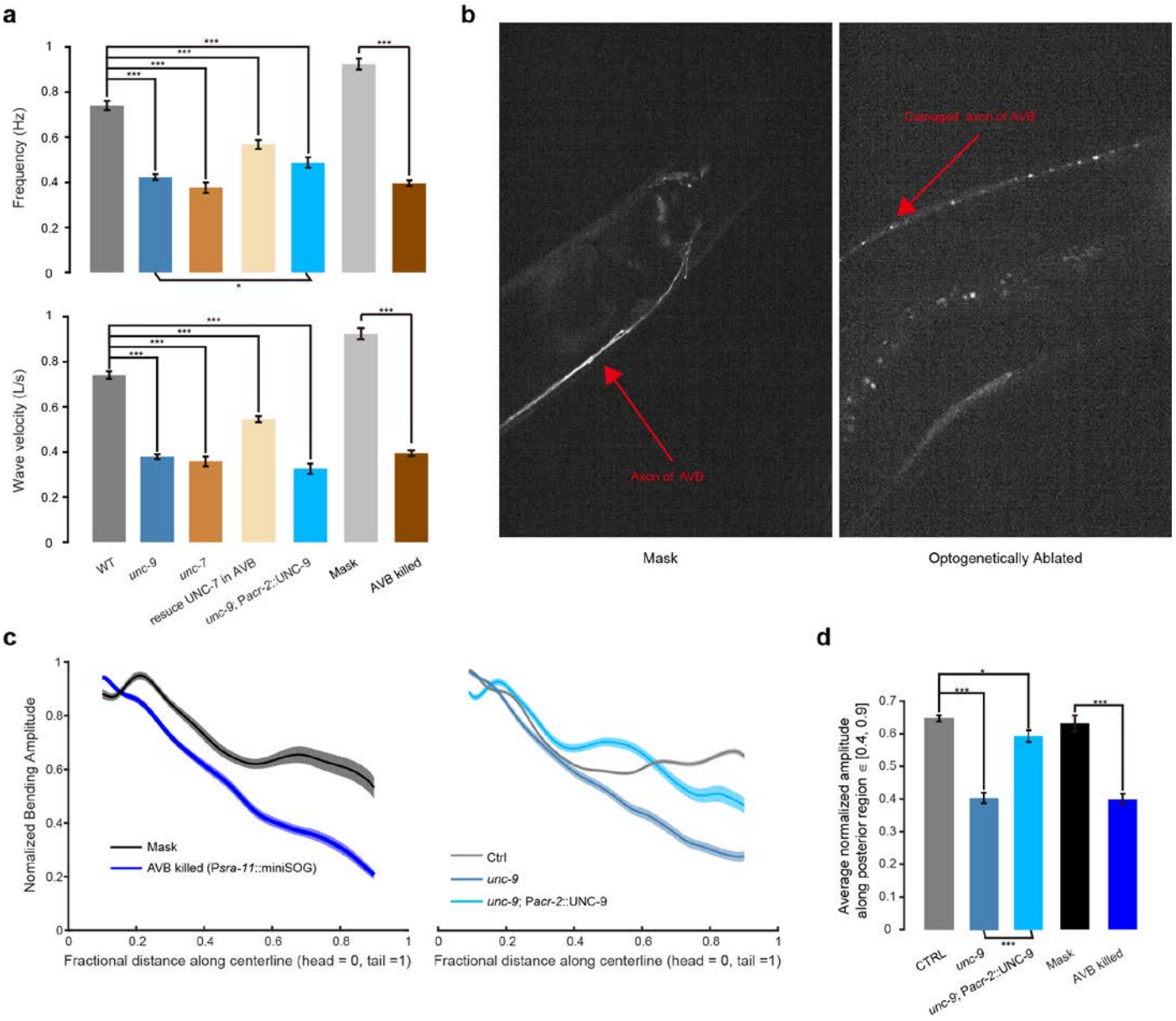

Supplementary Figure 1

AVB-B electrical couplings facilitate undulatory wave propagation during forward locomotion. Related to **Figure 1**.

(a) Locomotion kinematics of tested strains. Upper panel shows the comparison of undulation frequency in viscous medium (~ 1 Pa·s). Lower panel shows the comparison of wave velocity, calculated in worm body length per second (*L*/*s*). Error bars show s.e.m. *** p < 0.0001 with Bonferroni correction. Ctrl [N2; P*acr-5*::Arch; P*unc-4*::TWK-18(gf)], *n* = 13 worms, 107 measurements; *unc-7* mutant, [*unc-7*(*hp121*); P*acr-5::*Arch; P*unc-4*::TWK-18(gf)], *n* = 22 worms, 99 measurements; *unc-9* mutant [*unc-9*(*fc16*); P*acr-5*::Arch; P*unc-4::*TWK-18(gf)], *n* = 17 worms, 144 measurements; AVB ablated worm [P*glc-55(*B)::tom20::miniSOG::UrSL::wCherry], *n* = 13 worms, 80 measurements; Mask, *n* =12 worms, 96 measurements. **(b)** Comparison of AVB axon fluorsecence signals in mask and AVB ablated worms. Arrows indicate intact and damaged axons. **(c)** Left: Comparison of normalized bending amplitude along the worm body in mask and AVB ablated worms. We used a different transgenic strain (P*sra-11*::miniSOG) to drive the expression of miniSOG in AVB neurons. Right: Comparison of normalized bending amplitude along the worm body in CTRL, *unc-9* and UNC-9 rescue in B and A motor neurons [*unc-9*(*fc16*); P*acr-2*::UNC-9; P*acr-5*::arch]. Rescue UNC-9 in B and A motor neurons largely restored the posterior bending amplitude. Shaded regions show s.e.m. **(d)** Bending amplitude averaged over the posterior region ∈ [40, 90] of the worm body. ***p < 0.0001, *p < 0.05, two-sample t-test with Bonferroni correction. Error bars represent s.e.m. Ctrl, *n* = 13 worms, 105 measurements; unc-9 mutant, *n* = 17 worms, 93 measurements; UNC-9 rescue in motor neurons, *n* = 9 worms, 64 measurements. Mask, *n* = 5 worms, 28 measurements; AVB ablated worms (P*sra-11*::tomm20::miniSOG) *n* = 10 worms, 100 measurements.

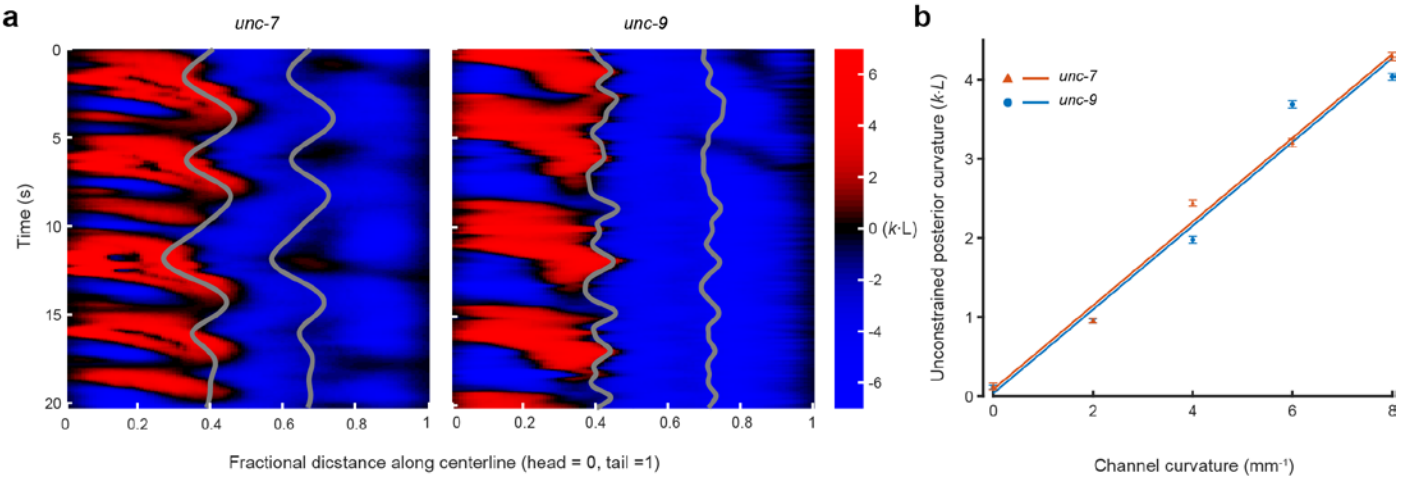

Supplementary Figure 2

AVB-B electrical couplings are not necessary for transducing the proprioceptive signals. Related to **Figure 2.**

(a) Representative kymograms show *unc-7*mutant [*unc-7*(hp121); P*unc-4::*TWK-18(gf)] and *unc-9*mutant [*unc-9*(fc16); P*unc-4::*TWK-18(gf)], in which worm mid bodies wereconstrained in microfluidic channel with definedcurvature (6 mm^{-1}). Gray lines indicate anterior and posterior boundaries of the channel. **(b)** Unconstrained posterior body curvature as a function of channel curvature. Each data point:*n* = 5 worms, error bars represent s.e.m. Blue and red lines are linear fit (R^2> 0.97).

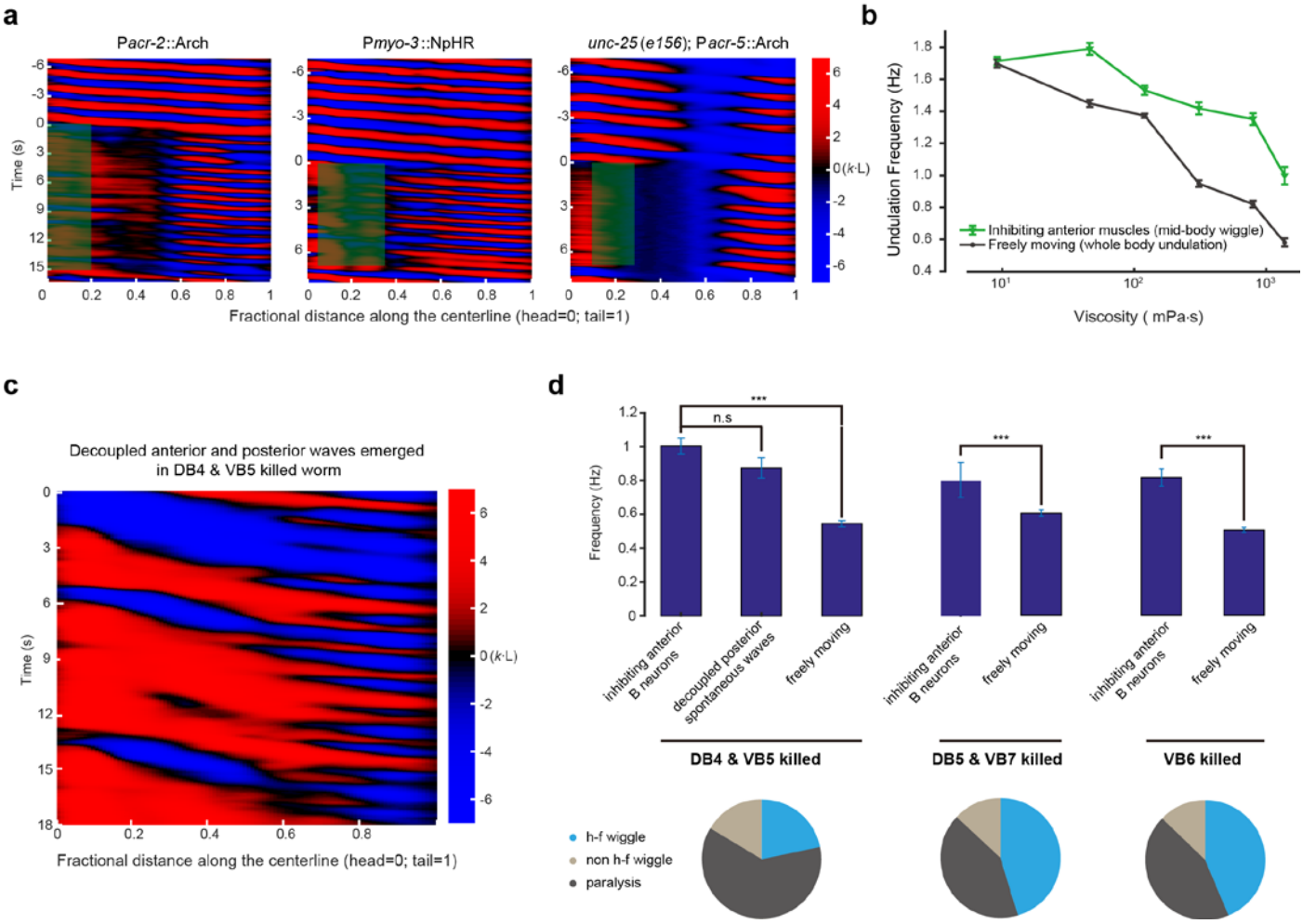

Supplementary Figure 3

Mid-body B motor neurons could intrinsically generate rhythmic activity. Related to **Figure 3**.

(a) Representative kymographs demonstrate that fast mid/posterior body undulatory waves could be induced by inhibiting anterior A & B motor neurons (P*acr-2*::Arch, 11 out of 25 measurements), inhibiting anterior muscles (P*myo-3*::NpHR, 52 out of 87 measurements) or by inhibiting anterior B motor neurons in GABA neurotransmitter deficient worms [*unc-25*(e156); P*acr-5*::Arch, 33 out of 45 measurements]. **(b)** Undulation frequency with the medium viscosity. Black, normal swimming worm; green, mid-body undulation when head and body were decoupled by inhibiting anterior muscle cells. Each data point represents mean and s.e.m from $n \geq 4$ worms. **(c)** Representative kymographs of a freely swimming worm in which DB4 & VB5 motor neurons were optogenetically ablated (P*acr-5*::tomm20::miniSOG). Decoupled anterior and posterior spontaneous waves could be observed. **(d)** Up, summary of undulation frequencies in B neurons selectively ablated worms. Several scenarios were compared. (1) Fast mid-body undulation induced by optogenetically inhibiting anterior B neurons. (2) Spontaneous posterior bending waves in DB4&VB5 ablated worms. (3) Freely swimming worms. Bottom, a pie chart summary of worm locomotor states across trials when anterior B neurons were optogenetically inhibited. State definitions can be found in the main text. Error bars show s.e.m., ***p<0.0001, n.s. p = 0.15, two-sample t-test. DB4 & VB5 killed n = 11 worms, DB5 & VB7 killed n = 8 worms, VB6 killed n = 9 worms.

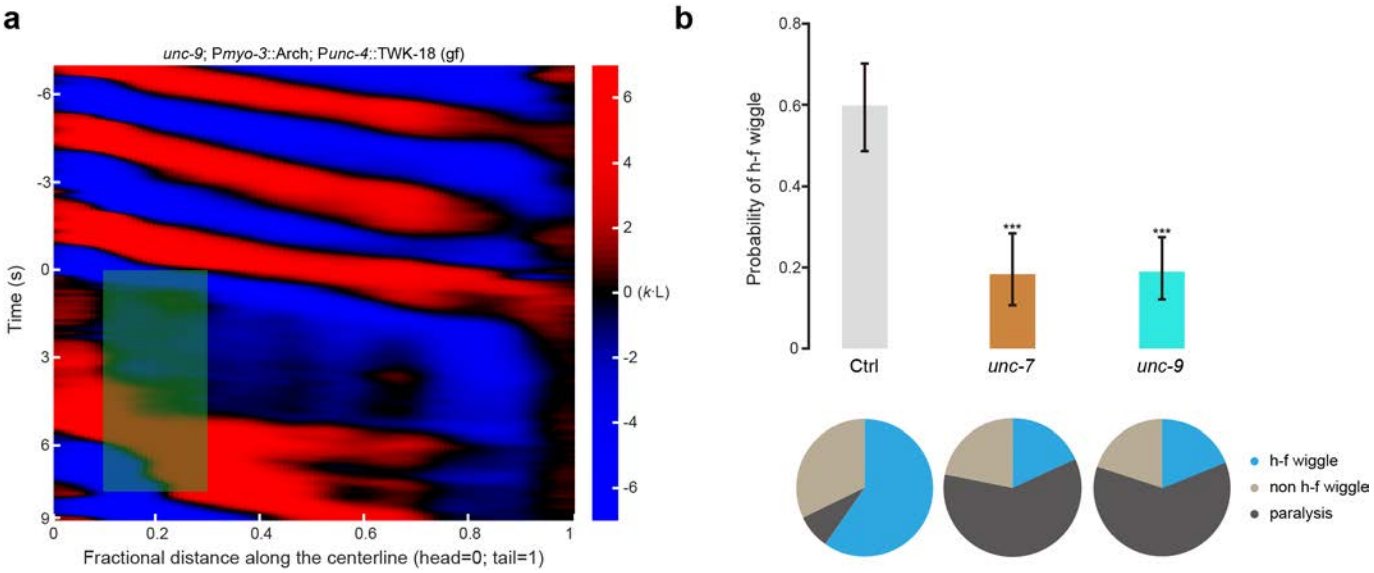

Supplementary Figure 4

AVB-B electrical couplings drive a bifurcation in B neuron dynamics. Related to **Figure 4**.

(a) Representative curvature kymographs of head-body-decoupled experiments in AVB-B gap junction deficient *unc-9*mutants [*unc-9*; P*myo-3*::Arch; P*unc-4*::TWK-18(gf)]. Anterior muscle cells were optogenetically inhibited to abolish the proprioceptive signals. **(b)** The probability for inducing high frequency mid-body undulation when head and body were decoupled by inhibiting anterior muscle cells. The pie chart summarizes the worm locomotor states across trials. State definitions can be found in the main text. Error bars indicate 95% binomial proportion confidence interval. ***p <0.0001, Chi-Square test. Ctrl [P*myo*-3::NpHR, *Punc-4::*TWK-18(gf)], n = 10 worms, 87 measurements. *unc-7* mutant [*unc-7(hp121);* P*myo*-3::Arch*; Punc-4::*TWK-18(gf)], *n* = 18 worms, 82 measurements. *unc-9* mutant [*unc-9(fc16);* P*myo*-3::Arch*; Punc-4::*TWK-18(gf)], *n* = 21 worms, 111 measurements.

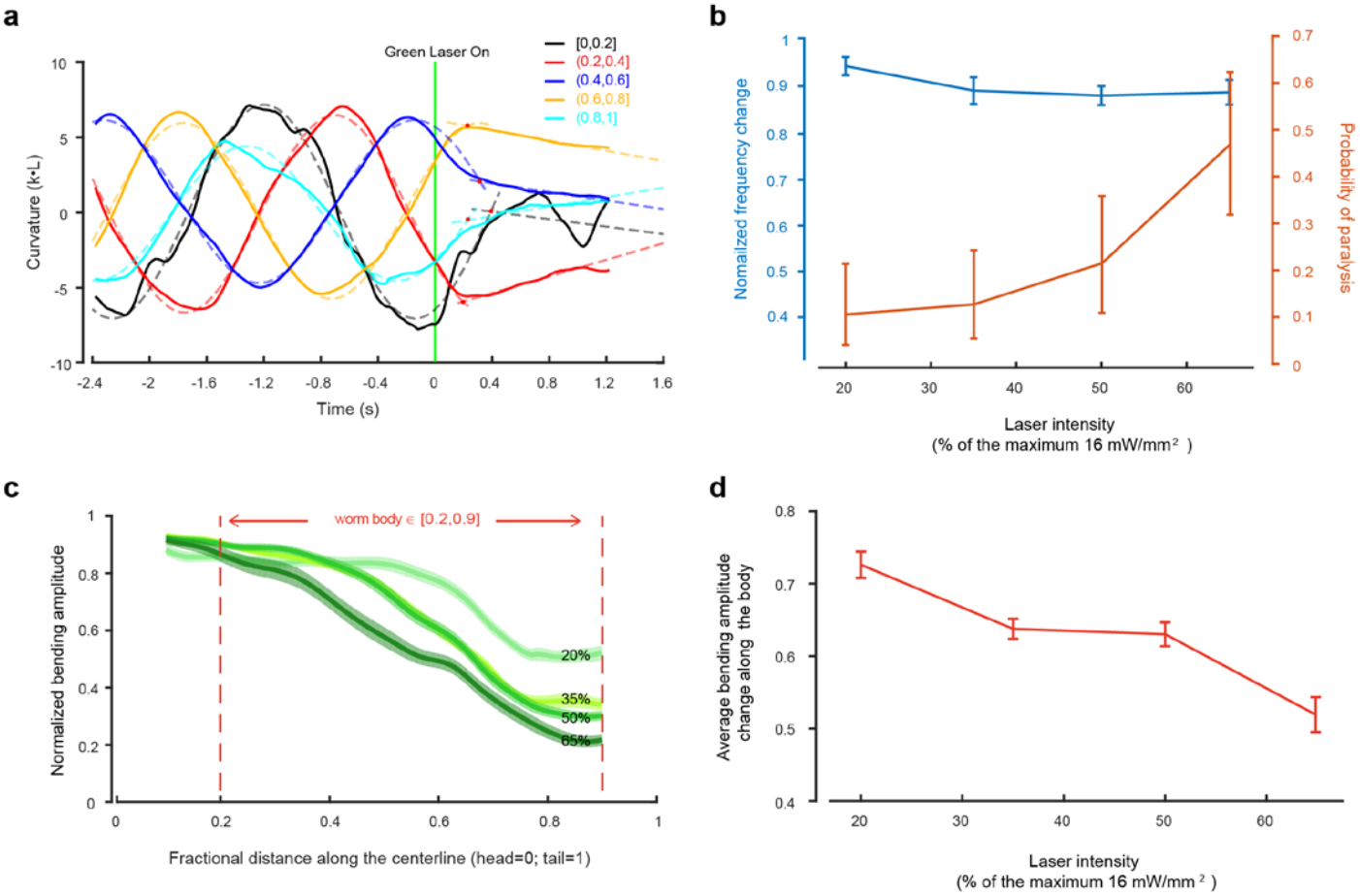

Supplementary Figure 5

Electrical couplings between motor neurons allow rapid and reciprocal interactions between head and body motor activity. Related to **Figure 5**.

(a) Estimate of reaction time when performing optogenetic inhibition of mid-body B motor neurons. First, we fit the regional curvature with a sinusoidal function right before green laser was on. Second, we performed a linear fit of regional curvature after optogenetic inhibition. The crossover point (red dot) stands for the wiggling-to-paralysis transition for each segment. Curvature was averaged over a defined color coded region, represented by a fractional distance along the worm coordinate (head = 0, tail = 1). **(b)** Dose-dependent effect on undulation frequency and on the efficacy for inducing whole-body paralysis when we optogenetically inhibited B motor neurons in a posterior body region ∈ [0.7, 0.9]. Error bars (blue), s.e.m. error bars (orange), 95% binomial proportion confidence interval. $n \geq 5$ worms for each data point. Maximum intensity: 16 mw/mm^2. **(c)** Dose dependent effect on bending amplitude along the worm body when we optogenetically inhibited B motor neurons in a posterior body region∈[0.7, 0.9]. Shaded regions are s.e.m. Maximum laser intensity: 16 mW/mm^2. **(d)** Average bending amplitude change along the body ∈ [0.2, 0.9] showing in (C). Error bars are s.e.m. Maximum laser intensity: 16 mW/mm^2.

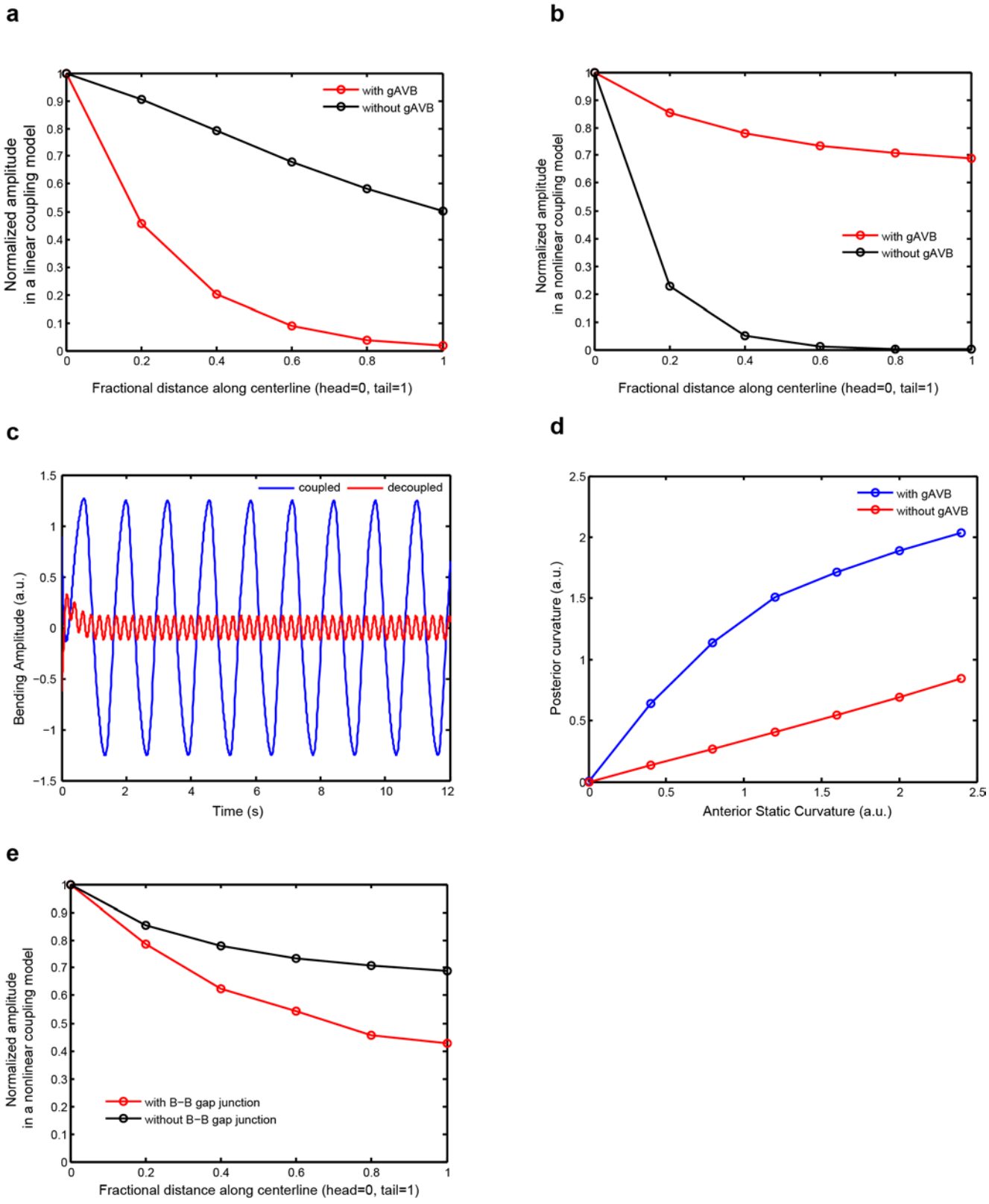

Supplementary Figure 6

Simulation results for linear or nonlinear proprioceptive coupling model. Related to **Figure 2** and **Figure 4**.

(a) Amplitude decay in the presence and absence of AVB-B gap junction in the linear proprioceptive coupling model. **(b)** Amplitude decay in the presence and absence of AVB-B gap junction in the nonlinear proprioceptive coupling model. **(c)** Bending dynamics of a mid-body segment when head and body are coupled or decoupled. **(d)** The curvature of the posterior body region when the anterior body

curvature is held at a constant value. **(e)** B-B gap junctions can deteriorate bending wave propagation. g_c, the strength of B-B gap junctions, is set to 20pS here.

Supplementary Videos

Supplementary Video 1 | *unc-7* mutant swam freely in viscous solution (~ 1 Pa·s viscosity). Despite wiggling its anterior body, the worm exhibited tail-dragging phenomenon.

Supplementary Video 2 | Optogenetically inhibiting anterior region of freely forward swimming WT worm can induce high-frequency wiggle in posterior region.

Supplementary Video 3 | Worm with UNC-7 rescued in AVB (P*sra-11*::UNC-7) swimming in viscous solution (~ 1 Pa·s viscosity) during head-and-body-decoupled experiment. Note the bending amplitude of posterior body and high-frequency wiggle in posterior region were restored.

Supplementary Video 4 | Optogenetically inhibiting mid-body B motor neurons in WT worm can paralyze the whole body.

Supplementary Video 5 | Optogenetically inhibiting mid-body B motor neurons in *unc-9* mutant only paralyzed the posterior region while the anterior region was still able to wiggle.

Supplementary Video 6 | Over-expression of UNC-9 in B motor neurons (P*acr-5*::UNC-9) caused whole body paralysis. Worms were incapable of propagating body undulations along its body.

Supplementary Experimental Procedures

Strain Information

Strain Name	Experiment	Genotype	Construct (plasmid no.) injection concentrations
WEN0315	B motor neurons inhibition experiments in WT	*wenIs0001; wenEx0315*	P*acr-5*::Arch::UrSL::wCherry (pJH2918);P*odr-1*::gfp P*unc-4*::TWK::18(gf)::UrSL::wCherry (pJH2108) 30 ng/µL; P*lin-14*::gfp 20 ng/µL; P*myo-3*::wCherry (pJH1774) 2.5 ng/µL
WEN0317	B motor neurons inhibition experiments in *unc-7* mutant; Microfluidic experiments	*wenIs0001 wenEx0317; unc-7(hp121)*	P*acr-5*::Arch:: UrSL::wCherry (pJH2918); P*odr-1*::gfp P*unc-4*::TWK::18(gf)::UrSL::wCherry (pJH2108) 30 ng/µL; P*lin-14*::gfp 20 ng/µL;P*myo-3*::wCherry (pjH1774) 2.5 ng/µL
WEN0304	B motor neurons inhibition experiments in *unc-9* mutant; Microfluidic experiments	*wenEx0304; hpEx2088; unc-9(fc16)*	P*acr-5*::Arch:: UrSL::wCherry (pJH2918) 30 ng/µL; P*lin-14*::gfp 20 ng/µL P*unc-4*::TWK::18(gf)::UrSL::wCherry (pJH2108) ; P*odr-1*::gfp
ZM7297	AVB ablation experiment	*hpIs331*;	P*lgc-55*(B)::tomm-20::miniSOG::UrSL::wCherry (pJH2890); lin-15 +
WEN0318	B motor neurons inhibition experiments upon AVB ablation; Microfluidic experiments	*wenIs0001; hpIs331;*	P*acr-5*::Arch::UrSL::wCherry (pJH2918);P*odr-1*::gfp P*lgc-55*(B)::tomm-20::miniSOG::UrSL::wCherry (pJH2890)
WEN0335	B motor neurons inhibition in *unc-7* mutants, with UNC-7 expression restored in AVB	*wenEx0335; wenIs0001; unc-7(hp121)*	P*unc-4*::TWK::18(gf)::UrSL::wCherry (pJH2108) 30 ng/µL; P*sra-11*::UNC-7(cDNA)::wCherry (pJH2037) 20 ng/µL; P*lin-14*::gfp 20ng/µL; P*myo-3*::wCherry 2.5 ng/µL P*acr-5*::Arch:: UrSL::wCherry (pJH2918); P*odr-1*::gfp
WEN0314	B moter neuron ablation; Microfluidic experiments	*wenIs0001; hpIs374;*	P*acr-5*::Arch:: UrSL::wCherry (pJH2918); P*odr-1*::gfp P*acr-5*::tomm-20::miniSOG::UrSL::wCherry (pJH2842)
WEN0001	B motor neurons inhibition experiments	*wenIs0001*	P*acr-5*::Arch::UrSL::wCherry (pJH2918); P*odr-1*::gfp
WEN0320	B motor neuron inhibition upon AVB ablation	*wenIs0001 wenEx0320*	P*acr-5*::Arch::UrSL::wCherry (pJH2918); P*odr-1*::gfp P*sra-11*::tomm-20::miniSOG::UrSL::wCherry (quan0065) 50 ng/µL; P*myo-3*::wCherry 2.5 ng/µL
ZM9275	A & B motor neurons inhibition	*hpIs615*	P*acr-2*(s)::Arch::wCherry (pJH3717)
ZX444.6	Muscle inhibition	*zxEx29; lin-15(n765ts)*	Pmyo-3::NpHR::ECFP; lin-15+
WEN0307	B motor neuron inhibition in *GABA* deficient mutants	*wenIs0001; unc-25(e156)*	P*acr-5*::Arch::UrSL::wCherry (pJH2918); P*odr-1*::gfp
ZM7796	B motor neuron ablation	*hpIs374*	P*acr-5*::tomm-20::miniSOG::UrSL::wCherry (pJH2842)
WEN0363	Muscle inhibition in *unc-7* mutants	wenEX0363; *unc-7(hp121)*	P*myo-3*::Arch::UrSL::wCherry (quan0124) 30 ng/ µl; P*unc-4*::TWK-18(gf)::UrSL::wCherry (pJH2108) 30 ng/µl
WEN0323	Muscle inhibition in *unc-9* mutants	*wenEx0323*; *unc-9(fc16)*	P*myo-3*::Arch::UrSL::wCherry (quan0124) 30 ng/µl; P*unc-4*::TWK-18(gf)::UrSL::wCherry (pJH2108) 30 ng/µl
WEN0337	*unc-9* mutants with restored expression in A and B motor neurons	*wenEx0337; unc-9(fc16)*	P*acr-2*::UNC-9::wCherry (pJH1897) 2 ng/µl; P*acr-5*::Arch:: UrSL::wCherry (pJH2918) 30 ng/µl
WEN0366	Over-expression of UNC-9 in B motor neurons	*wenEx0366*	P*acr-5*::Arch:: UrSL::wCherry (pJH2918) 30 ng/µl; P*acr-5*::UNC-9 (pJH2140) 30 ng/µl

A linear proprioceptive coupling model for undulatory wave propagation in *C. elegans*

We first developed a linear coupling model to simulate the wave propagation within the body of *C. elegans*. The head motor circuit contains an oscillator that dominates the rhythmic motion of the whole body. Other segments cannot oscillate by themselves. They oscillate according to the proprioceptive input from the anterior segment. This simple model is phenomenological, for it does not simulate the detailed dynamics of individual neurons. Instead, it aims at elucidating several key properties of wave propagation based on linear proprioceptive coupling.

The dynamics of the head oscillator is dictated by the following equations.

$$\begin{cases} \tau_s \dfrac{dv}{dt} = v - \beta v^3 - \mathrm{a}k \\ \tau_h \dfrac{du}{dt} = -u + v \\ \tau_\eta \dfrac{dk}{dt} = -k + \alpha_{max} * u/b\,, \end{cases} \qquad (S1)$$

where v describes relative neural activity of head motor neurons. It is not the real membrane potential, but a variable representing the dorsal-ventral bias of neural activity. It has a value between -1 and 1, or in a slightly broader region. When dorsal B neurons have a stronger neural activity than ventral ones, $v > 0$, and vice versa. $\alpha_{max} * u$ is the maximum torque that the muscle can generate, and u is a dimensionless variable. b is the bending modulus of the worm body and k is the curvature of the segment. The second equation relates neural activity and muscle torque. The nonlinear term, $v - \beta v^3$, as well as the negative sensory feedback term $-\mathrm{a}k$ are critical for generating head oscillation. The last equation relates muscle torque and body shape change in a defined segment [1, 2]. τ_η is a time constant proportional to the viscosity η of the medium. In the case of viscous medium, namely large η, $\tau_\eta \gg \tau_h, \tau_\eta \gg \tau_s$, the period of such a relaxation oscillator is largely determined by τ_η. As a result, the undulation frequency would decrease with viscosity, which has been observed experimentally [1].

Apart from the head, we divide the worm body into 5 segments (the number of segments are not essential for our theoretical argument). These segments have a different dynamics, which is described as follows.

$$\begin{cases} C \dfrac{dv_i}{dt} = g_m(-v_i + ck_{i-1}) - gv_i \\ \tau_h \dfrac{du_i}{dt} = -u_i + v_i \qquad i = 2,3,4,5,6 \\ \tau_\eta \dfrac{dk_i}{dt} = -k_i + \alpha_{max} * v_i/b\,. \end{cases} \qquad (S2)$$

Here k_{i-1} is the curvature of the anterior segment. The term $-gv_i$ denotes the contribution of AVB-B gap junction to the membrane potential of B neurons. More essentially, it should be $-g(v_i - v_{AVB})$.For simplicity, we set $v_{AVB} = 0$. On the one hand, the membrane potential of AVB remains nearly constant during forward locomotion. On the other hand, setting it to 0 can eliminate the bias between dorsal and ventral sides and avoid unnecessary complexity in our model. Here C is the membrane capacitance, g_m is the leaky membrane conductance.

Eqs. (S1) and (S2) arise naturally from a biologically more realistic model where dorsal and ventral activities are treated separately. The equations now become

$$\begin{cases} \tau_s \dfrac{dv_d}{dt} = v_d - \beta {v_d}^3 - \mathrm{a}k \\ \tau_h \dfrac{du_d}{dt} = -u_d + v_d \\ \tau_s \dfrac{dv_v}{dt} = v_v - \beta {v_v}^3 + \mathrm{a}k \qquad Head \\ \tau_h \dfrac{du_v}{dt} = -u_v + v_v \\ \tau_\eta \dfrac{dk}{dt} = -k + \alpha_{max} * (u_d - u_v)/b \end{cases} \qquad (S3)$$

$$\begin{cases} C\dfrac{dv_{di}}{dt} = g_m(-v_{di} + ck_{i-1}) - gv_{di} \\ \tau_h\dfrac{du_{di}}{dt} = -u_{di} + v_{di} \\ c_m\dfrac{dv_{vi}}{dt} = g_m(-v_{vi} - ck_{i-1}) - gv_{vi} \quad Other\ segments, i = 2,3,4,5,6 \\ \tau_h\dfrac{du_{vi}}{dt} = -u_{vi} + v_{vi} \\ \tau_\eta\dfrac{dk_i}{dt} = -k_i + \alpha_{max} * (u_{di} - u_{vi})/b \end{cases} \quad (S4)$$

If we subtract "dorsal equations" from "ventral equations", Eqs. (S1) and (S2) will be derived: dorsal activity and ventral activity are anti-phased, or namely $v_d = -v_i$ and $v_{di} = -v_{vi}$. Simulation using Eqs. (S3) and (S4) did not show any essential difference compared to the simulation using Eqs. (S1) and (S2).

The linear proprioceptive coupling model makes two key predictions that can be tested experimentally. First, abolishing the head motor activity should abolish the undulatory wave propagation. However, we observed high frequency undulation emerged from the mid-body of the worm when head and body were decoupled in our experiments. Second, simulation suggests AVB-B gap junction coupling would deteriorate bending wave propagation (**Fig. 2d** and **Supplementary Fig. 6a**). However, experimental data revealed the opposite. Therefore, we conclude that the linear coupling model is oversimplified and must be modified.

Parameters used in simulation:

$$\mathrm{a} = 0.385\ mm, \alpha_{max}/b = 2mm^{-1}, \beta = 1.$$
$$c_m = 4.5\ \mathrm{nF}, g_m = 100\ pS, c = 0.6\ mm, \tau_h = 75ms, \tau_s = 75ms$$
$$\tau_\eta = \frac{C_N}{b}\left(\frac{2\pi}{\lambda}\right)^4 \approx \frac{30\eta}{b}\left(\frac{2\pi}{\lambda}\right)^4, \quad b = 9.5 \times 10^{-14}\mathrm{N} * m^2, \lambda = 1mm.$$
$$\eta = 1\mathrm{Pa} * \mathrm{s}.$$

2

An analytical solution to the linear proprioceptive coupling model

To gain a deeper insight into the amplitude decay during wave propagation, we have developed an analytical understanding for the linear coupling model by transforming Equation (S2) into a continuous form.

The dynamic equations for wave propagation can be rewritten as follows.

$$\begin{cases} C\dfrac{\partial v}{\partial t} = g_m(-v + ck(x-l)). \\ \tau_\eta\dfrac{\partial k}{\partial t} = -k + \alpha_{max}v/b\,. \end{cases} \quad 0 < x < L - l \quad (S6)$$

In the first equation, the second term, $ck(x-l)$, denotes how proprioceptive couplings drive the change of neural activity in motor neurons (Wen et al., 2012). l is the characteristic length of proprioception. The second equation relates the change of body shape with neural activity. Here, for simplicity, we dropped the equation that relates neural activity and muscle torque in Eqs. (S2). The delay time between neural activity and muscle torque, characterized by τ_h, was absorbed by the time constant τ_η in Eq. (S6). We shall assume a harmonic motion to describe the dynamics of the head. The $v(\mathrm{x})$ and $k(x)$ can be written as

$$\begin{cases} v = v_0 \exp\left(i\left(\dfrac{2\pi x}{\lambda} - \omega t\right)\right). \\ k = k_0 \exp\left(i\left(\dfrac{2\pi x}{\lambda} - \omega t\right)\right). \end{cases} \quad -l < x < 0 \quad (S7)$$

The neural activity and curvature are not in-phase. But we can absorb the phase factor into coefficents v_0 and k_0, which are all complex numbers.

We postulate that the solution is also sinusoidal, namely

$$\begin{cases} v = V(x) \exp\left(i\left(\dfrac{2\pi x}{\lambda} - \omega t\right)\right). \\ k = K(x) \exp\left(i\left(\dfrac{2\pi x}{\lambda} - \omega t\right)\right). \end{cases} \quad 0 < x < L - l \quad (S8)$$

Substituting into Eqs. (S6), and defining $\tau_c = C/g_m$, we have

$$-i\omega\tau_c V(x) = -V(x) + c\exp\left(-i\frac{2\pi l}{\lambda}\right)K(x-l). \quad (S9)$$

$$-i\omega\tau_\eta K(x) = -K(x) + \alpha_{max}V(x)/b. \qquad \text{(S10)}$$

Replacing $K(x-l)$ with $K(x) - K'(x)l + K''(x)l^2/2$, and using $l \ll \lambda$, we found

$$\frac{c\alpha_{max}l^2}{2(1-i\omega\tau_\eta)b}V''(x) - \frac{c\alpha_{max}l}{(1-i\omega\tau_\eta)b}V'(x) + \left(i\omega\tau_c - 1 + \frac{c\alpha_{max}}{(1-i\omega\tau_\eta)b}\right)V(x) = 0. \qquad \text{(S11)}$$

The solution is

$$V(x) = v_0\, exp\left(-\frac{B+\sqrt{B^2-4AC}}{2A}x\right), \qquad \text{(S12)}$$

where

$$A = \frac{c\alpha_{max}l^2}{2(1-i\omega\tau_\eta)b}, \quad B = -\frac{c\alpha_{max}l}{(1-i\omega\tau_\eta)b}, \quad C = i\omega\tau_c - 1 + \frac{c\alpha_{max}}{(1-i\omega\tau_\eta)b}. \quad (S13)$$

Thus the decaying length constant satisfies

$$1/\xi = \mathrm{Re}\frac{B+\sqrt{B^2-4AC}}{2A}. \qquad \text{(S14)}$$

Expanding it to power series of ω and only preserving low order terms, we have

$$\xi = \frac{l}{1-\frac{c\alpha_{max}}{b} + \omega^2\left(\frac{c\alpha_{max}(\tau_c^2+\tau_\eta^2)}{2b} + \left(\frac{c\alpha_{max}}{b}-1\right)\tau_c\tau_\eta\right)}. \quad (S15)$$

According to earlier works [1],

$$\tau_\eta = \frac{C_N}{b}(\frac{2\pi}{\lambda})^4 \approx \frac{30\eta}{b}\left(\frac{2\pi}{\lambda}\right)^4. \qquad (S16)$$

The time constant τ_η increases with the viscosity of the medium η, and the decay length constant ξ would decrease with η.

To the leading order, the decay length constant is given by

$$\xi \approx \frac{l}{1-\frac{c\alpha_{max}}{b}}. \qquad \text{(S19)}$$

When we incorporate electrical couplings between AVB-B neurons into this model, the equations become

$$\begin{cases} \tau_c\frac{\partial v}{\partial t} = -v - gv/g_m + ck(x-l). \\ \tau_\eta\frac{\partial k}{\partial t} = -k + \alpha_{max}v/b\,. \end{cases} \quad 0 < x < L-l, \qquad \text{(S18)}$$

where g denotes the strength of the gap junction.In this case, the decay length constant becomes

$$\xi \approx \frac{l}{1-\frac{g_m c\alpha_{max}}{(g+g_m)b}}, \qquad \text{(S19)}$$

which further deteriorates the bending wave propagation. This prediction is inconsistent with the experimental observations.

A detailed nonlinear proprioceptive coupling model

The discrepancy between experimental data and our simple linear model forces us to develop a modified nonlinear coupling model. The head oscillator has the same functional form as that in the linear coupling model:

$$\begin{cases} \tau_s\frac{dv_d}{dt} = v_d - \beta {v_d}^3 - \mathrm{a}k \\ \tau_h\frac{dn_d}{dt} = -n_d + v_d \\ \tau_s\frac{dv_v}{dt} = v_v - \beta {v_v}^3 + \mathrm{a}k \\ \tau_h\frac{dn_v}{dt} = -n_v + v_v \\ \tau_\eta\frac{dk}{dt} = -k + \alpha_{max} * (n_d - n_v)/b \end{cases} \qquad (S20)$$

Here the subscripts 'd' and 'v' denote dorsal and ventral sides respectively, $\alpha_{max} * (n_d - n_v)$ is the maximal torque that the muscle can generate.

For all the other segments, our model will incorporate the experimental observations that motor neurons can generate intrinsic oscillations when head and body are decoupled, and when AVB and B neurons are electrically coupled ($g > 0$).The intrinsic membrane properties in B motor neuron remain unknown because of the extraordinary difficulty in performing whole-cell patch clamp recording in motor neurons (cell body ~ 1-2 μm in diameter). For simplicity, we developed a classic phenomenological model based on persistent Ca^{2+} and K^+ conductances, which is derived from a simplified version of the $I_{Na} - I_K$ model [3].

The dynamic equations are written in the following form.

$$\begin{cases} C\frac{dV_d}{dt} = -g_L(V_d - E_L) - g_{Ca}m(V_d) * (V_d - E_{Ca}) - g_K n_d * (V_d - E_K) + c'k' + g(V_0 - V_d) \\ \tau_c \frac{dn_d}{dt} = -n_d + n(V_d) \\ C\frac{dV_v}{dt} = -g_L(V_v - E_L) - g_{Ca}m(V_v) * (V_v - E_{Ca}) - g_K n_v * (V_v - E_K) - c'k' + g(V_0 - V_v) \\ \tau_c \frac{dn_v}{dt} = -n_v + n(V_v) \\ \tau_u \frac{dM_d}{dt} = -M_d + M(V_d) - M(V_v) \\ \tau_u \frac{dM_v}{dt} = -M_v + M(V_v) - M(V_d) \\ \tau_\eta \frac{dk}{dt} = -k + \alpha'_{max}/b * (M_d - M_v) \end{cases} . \quad (S21)$$

k' is the curvature of the neighboring anterior segment; $m(V), n(V)$ are voltage dependent gating variables; $M(V)$ relates cell membrane potential and muscle torque.

$$m(V) = \frac{1}{1 + \exp(\frac{V - V_m}{\theta_m})}, n(V) = \frac{1}{1 + \exp(\frac{V - V_n}{\theta_n})}, M(V) = \frac{1}{1 + \exp(\frac{V - V_{mus}}{\theta_{mus}})}. \quad (S22)$$

$g(V_0 - V)$ is the current flowing through the gap junction between AVB neurons and B neurons, and V_0 is the membrane potential of the AVB neurons, held at a constant value.

The terms $-M(V_v)$ and $-M(V_d)$ in the third and the fourth equation of (S21) reflect contralateral inhibition from D-type GABAergic motor neurons: dorsal D neurons can be activated by ventral B neurons and thereby inhibit dorsal muscle activity, and vice versa.

We were simulating 6 segments (including the head), similar to that in a linear coupling model. The parameter values are listed below.

$$\tau_s = 50.0nF, \quad \tau_h = 200ms, \quad \mathrm{C} = 3.0\mathrm{nF}, \ \tau_c = 30ms, \tau_u = 85ms.$$
$$\tau_\eta = \frac{C_N}{b}(\frac{2\pi}{\lambda})^4 \approx \frac{30\eta}{b}\left(\frac{2\pi}{\lambda}\right)^4, \quad b = 9.5 \times 10^{-14}\mathrm{N} * m^2, \lambda = 1mm.$$
$$g_m = 100pS, g_L = 100pS, \quad g_{Ca} = 400pS, g_K = 500pS.$$
$$\mathrm{a} = 0.385mm, \beta = 1, \mathrm{c}' = 5\mathrm{mA/mm}, \alpha_{max}/b = 10mm^{-1}, \alpha'_{max}/b = 2.1mm^{-1}.$$
$$E_L = -60\mathrm{mV}, E_{Ca} = 60mV, E_K = -70mV, E_0 = -60mV, V_0 = -20mV.$$
$$V_m = -29mV, V_n = -55mV, V_{mus} = -45mV.$$
$$\theta_m = 10.25mV, \theta_n = 20mV, \theta_{mus} = 10mV.$$
$$\eta = 1\mathrm{Pa} * \mathrm{s}.$$

Comparing the cases $g = 0$ and $g = 100\mathrm{pS}$, we find that gap junction coupling between AVB and B neurons could equalize the bending amplitude **(Supplementary Fig. 6b)**. High frequency oscillation within middle segments can also be generated when head and body are decoupled (**Supplementary Fig. 6c**). When we hold an anterior segment at a static curvature, the neighboring posterior segment will follow (**Supplementary Fig. 6d**). These properties were consistent with our experimental observations.

Finally, we incorporate electrical coupling between B neurons into our model. The dynamic equations now become

$$C\frac{dV_d}{dt} = -g_L(V_d - E_L) - g_{Ca}m(V_d) * (V_d - E_{Ca}) - g_K n_d * (V_d - E_K) + c'k' + g(V_0 - V_d) - g_c\left(2V_d - V_{d(+1)} - V_{d(-1)}\right).$$
$$C\frac{dV_v}{dt} = -g_L(V_v - E_L) - g_{Ca}m(V_v) * (V_v - E_{Ca}) - g_K n_v * (V_v - E_K) - c'k' + g(V_0 - V_v) - g_c\left(2V_v - V_{v(+1)} - V_{v(-1)}\right). \quad (S23)$$

where $V_{d/v(+1)}$ and $V_{d/v(-1)}$ denote the membrane potentials of neighboring posterior dorsal/ventral and anterior dorsal/ventral B motor neurons.

We found that the amplitude decay became worse in the presence of strong B-B gap junctions (**Supplementary Fig. 6e**), consistent with experimental observation that overexpression of UNC-9 in B motor neurons would deteriorate coordinated locomotion (**Supplementary Video 6**). Could B-B gap junctions have other motor functions? As our optogenetic experiments suggested (**Fig. 5**), gap junctions between motor neurons could mediate the frequency of the head oscillator. However, a detailed model requires a deep understanding of how the head motor circuit operates. Our current head oscillator model is purely phenomenological, and a better model would be developed in a future work where all circuit components in the head motor circuit can be carefully defined and experimentally identified.

Supplementary References

1. Fang-Yen, C*., et al.* Biomechanical analysis of gait adaptation in the nematode Caenorhabditis elegans. *P Natl Acad Sci USA* **107**, 20323-20328 (2010).
2. Wen, Q*., et al.* Proprioceptive coupling within motor neurons drives C. elegans forward locomotion. *Neuron* **76**, 750-761 (2012).
3. Izhikevich, E.M. *Dynamical systems in neuroscience : the geometry of excitability and bursting* (MIT Press, Cambridge, Mass., 2007).